

RICE UNIVERSITY

**Design of a Fast, Efficient and Controlled DNA  
Shearing System Based on Lateral Acoustic Waves**

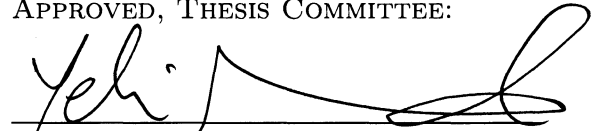
by

**Kapil Dev**

A THESIS SUBMITTED  
IN PARTIAL FULFILLMENT OF THE  
REQUIREMENTS FOR THE DEGREE

**Master of Science**

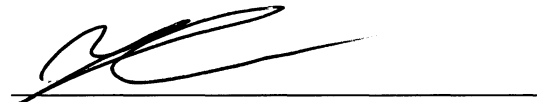
APPROVED, THESIS COMMITTEE:



Yehia Massoud, Chair  
Professor of Electrical and Computer  
Engineering and Computer Science



Farinaz Koushanfar  
Assistant Professor of Electrical and  
Computer Engineering and Computer  
Science



Lin Zhong  
Associate Professor of Electrical and  
Computer Engineering and Computer  
Science

Houston, Texas

December, 2011

## ABSTRACT

Design of a Fast, Efficient and Controlled DNA Shearing System Based on Lateral Acoustic Waves

by

Kapil Dev

With the continuous research and advances in Deoxyribonucleic acid (DNA) sequencing technologies, the need for an efficient DNA shearing system has increased more than ever before. In this thesis, we propose a fast, efficient and controlled DNA shearing system based on a uniquely designed ultrasonic transducer, called Fresnel Annular Sector Actuator (FASA). Based on the simulation and experimental results, a circular array of four 90°-FASA elements is chosen as the basic unit for the proposed shearing system. DNA is successfully sheared from 300 to 1500 base-pair lengths. The shearing performance of the system is independent of the source of DNA over a large range of concentrations of the DNA. Finally, multiple FASA elements, excited by separate RF-signals, are used to increase the throughput of the proposed shearing system.

## Acknowledgments

First and foremost, I would like to thank my thesis advisor, Professor Yehia Massoud, for his continuous encouragement and support during this research work. His invaluable suggestions and extreme enthusiasm helped me in persistently working on the problems I faced during the research. I feel honored and privileged to work under the tutelage of Professor Yehia Massoud.

Next, I would like to thank my thesis committee members, Professor Farinaz Koushanfar and Professor Lin Zhong for providing invaluable comments and suggestions on this research work.

I am indebted to the engineers and scientists at Microsonic Systems (Microsonics) San Jose, CA. In particular, I am thankful to Vibhu Vivek, Babur Hadimioglu, Smriti Sharma, Parvez Deshmukh, Steven Horwitz, and Peter Leigh for helping me in different ways to perform DNA shearing experiments. I feel lucky to get an internship opportunity at Microsonics. Most of the practical work presented in this thesis was performed there. I also want to extend my sincere appreciation to Brian Jones and Ma Phiengsai for helping me in assembling electrical circuits, piezoelectric transducers and building test-fixtures for performing DNA shearing experiments

I am highly grateful to all the colleagues of Nanoelectronic Systems Lab (NSL) at Rice University. In particular, I am privileged to share the lab with extremely talented people, like Sami El Smaili, Vikas Singal, Ahmad Hammoudi, and Keith Wilhelm, who not only used to be available for any-time technical discussions but also are very good friends of mine.

Finally, I want to thank my parents and sister for continuously providing me love and encouragement throughout these years. This thesis is dedicated to my parents.

# Contents

Abstract	ii
Acknowledgments	iii
List of Illustrations	vi
List of Tables	x
<b>1 Introduction</b>	<b>1</b>
<b>2 DNA Shearing</b>	<b>7</b>
2.1 DNA Structure . . . . .	7
2.2 DNA Shearing Methods . . . . .	8
2.2.1 Related Work . . . . .	9
2.2.2 Our Research Work . . . . .	14
<b>3 Theory and Modeling of Piezoelectric Transducers</b>	<b>16</b>
3.1 Piezoelectric Effect . . . . .	16
3.2 One-dimensional Model of a Piezoelectric Slab Excited in its Thickness Mode . . . . .	17
<b>4 Acoustic Field Due to Different Piezoelectric Transducers: Simulation Based Analysis</b>	<b>26</b>
4.1 Plane/Flat Piston Transducers With Different Electrode Patterns . .	27
4.2 Circular Plate Transducer . . . . .	29
4.3 Plane Transducer With Full-ring Electrode Pattern . . . . .	35
4.3.1 Acoustic Fresnel Lens . . . . .	35

4.3.2	Acoustic Field due to 360° Fresnel Lens . . . . .	36
4.4	Piezoelectric Transducer with Sectored Annular Electrodes . . . . .	39
4.4.1	270° Sectored Annular Transducer . . . . .	40
4.4.2	180° Sectored Annular Transducer . . . . .	42
4.4.3	90° Segmented FASA Element: the Basic Unit of DNA Shearing System . . . . .	43
4.4.4	Phased-Array Fresnel Annular Sector Actuators (FASAs) . . . . .	46
<b>5</b>	<b>Fabrication and Characterization of Piezoelectric FASA Element</b>	<b>50</b>
5.1	Photo-lithography Based Fabrication Process . . . . .	50
5.2	Characterization . . . . .	51
5.3	Equivalent Electrical-Circuit of Piezoelectric Transducer Based on its Impedance Characterization . . . . .	53
<b>6</b>	<b>Complete Architecture of Proposed DNA Shearing Sys- tem</b>	<b>56</b>
6.1	Electrical Domain . . . . .	56
6.2	Piezoelectric Domain . . . . .	60
6.3	Acoustic-fluid Interaction Domain . . . . .	60
<b>7</b>	<b>Experimental Results</b>	<b>63</b>
7.1	DNA Fragment Analysis Tools . . . . .	63
7.2	DNA Shearing Protocol and DNA Shearing Results . . . . .	65
<b>8</b>	<b>Conclusions and Future Work</b>	<b>75</b>
	<b>Bibliography</b>	<b>79</b>

# Illustrations

1.1	Genome based disease detection and treatment. . . . .	3
2.1	Different representations of DNA molecule: (a) chemical structure of DNA [35] (b) double-helix structure of DNA [36] (c) long entangled DNA. . . . .	8
2.2	Unsheared DNA and sheared DNA fragments . . . . .	9
2.3	Hydroshear System . . . . .	11
2.4	DNA shearing using lateral shear waves . . . . .	15
3.1	An acoustic medium of finite thickness, $d$ , with waves propagating in $+z$ and $-z$ directions. . . . .	17
3.2	Electrical excitation of piezoelectric slab in thickness mode. . . . .	21
3.3	Mason model equivalent circuit of a finite thickness piezoelectric plate	24
4.1	Electrodes (in blue color) of different shapes patterned on piezoelectric square block (in green color): (a) circular plate electrode (b) full-ring electrode (c) 270° FASA element with two rings (d) 180° FASA element with two rings (e) 90° FASA element with two rings. . . . .	28
4.2	Computation of acoustic field at a point P due to circular piezoelectric slab. . . . .	30

4.3	(a) Circular-plate electrode of $4mm$ radius; (b) vertical-component of particle displacement ( $u_z$ ); (c) radial-component of particle displacement ( $u_r$ ); (d) circumferential-component of particle displacement ( $u_\psi$ ). . . . .	33
4.4	Natural focal length versus diameter of the transducer at 4MHz in water. . . . .	34
4.5	Top view, cross-sectional view and ring-radii of a three-ring Fresnel lens	35
4.6	(a) Full ring ( $360^\circ$ ) electrode with $13mm$ focal length; (b) vertical-component of particle displacement ( $u_z$ ); (c) radial-component of particle displacement ( $u_r$ ); (d) circumferential-component of particle displacement ( $u_\psi$ ). . . . .	39
4.7	(a) $270^\circ$ FASA ring electrode with $13mm$ focal length; (b) vertical-component of particle displacement ( $u_z$ ); (c) radial-component of particle displacement ( $u_r$ ); (d) circumferential-component of particle displacement ( $u_\psi$ ). . . . .	41
4.8	(a) $180^\circ$ FASA ring electrode with $13mm$ focal length; (b) vertical-component of particle displacement ( $u_z$ ); (c) radial-component of particle displacement ( $u_r$ ); (d) circumferential-component of particle displacement ( $u_\psi$ ). . . . .	43
4.9	(a) $90^\circ$ FASA ring electrode with $13mm$ focal length; (b) vertical-component of particle displacement ( $u_z$ ); (c) radial-component of particle displacement ( $u_r$ ); (d) circumferential-component of particle displacement ( $u_\psi$ ). . . . .	45
4.10	Particle displacement for different sector angles (a)-(c) $u_z$ , $u_r$ , $u_\psi$ per unit electrode area; (d)-(f) Absolute $u_z$ , $u_r$ , $u_\psi$ . . . . .	46
4.11	Proposed piezoelectric transducer structure based on array of four $90^\circ$ Fresnel annular actuators. . . . .	47

4.12	Particle displacement due to an array of four 90° sectored annular transducers: (a)-(d) $u_z$ : <i>shift=0</i> , $\lambda$ , $3\lambda$ , $5\lambda$ ; (e)-(h) $u_r$ : <i>shift=0</i> , $\lambda$ , $3\lambda$ , $5\lambda$ ; (i)-(l) $u_\psi$ : <i>shift=0</i> , $\lambda$ , $3\lambda$ , $5\lambda$ . . . . .	49
5.1	$S_{11}$ plots for a sample piezoelectric FASA element plotted using Agilent E5061B network-analyzer. (a) log magnitude plot; (b) Smith impedance plot. . . . .	52
5.2	$S_{11}$ plot of a fresnel annular sector actuator patterned on a transducer obtained from Piezo Systems, Inc. . . . .	53
5.3	Resistance (R), reactance (X) and impedance (Z) plots of a Fresnel annular sector actuator designed on a transducer obtained from Piezo Systems, Inc. . . . .	54
5.4	Circuit models for FASA element at different operating frequencies. (a) $f < f_s$ ; (b) $f_s < f < f_p$ ; (c) $f > f_p$ . . . . .	55
6.1	Block diagram of the proposed DNA shearing system . . . . .	56
6.2	Combined clock: logical AND of fast RF clock (MHz) and slow clock at repetition rate . . . . .	57
6.3	Circuit diagram of class-E amplifier used to generate RF-signal for exciting the transducer [52]. . . . .	59
6.4	DNA shearing in action . . . . .	62
7.1	(a) Gel-electrophoresis system [55] (b) gel-image of Lambda DNA(48kb)[Concentration 5ng/ $\mu$ L] sheared to different peak fragment sizes using the proposed shearing system . . . . .	67
7.2	Agilent Bioanalyzer plots for the four shearing experiments (a) mean fragment size: 1850; (b) mean fragment size: 1350; (c) mean fragment size: 700; (d) mean fragment size: 370. . . . .	68



7.3	Agilent Bioanalyzer plots for a 50uL DNA sample sonicated for different time durations (a) 10 mins; (b) 20 mins; (c) 30 mins; (d) 40 mins; (e) 50 mins; (f) 60 mins. . . . .	70
7.4	Agilent Bioanalyzer plots for a 100uL DNA sample sonicated for different time durations (a) 10 mins; (b) 20 mins; (c) 30 mins; (d) 40 mins; (e) 50 mins; (f) 60 mins. . . . .	71
7.5	Shearing results on Lambda and Genomic DNA for 15 mins, 30 mins, and 1 hour sonication time. . . . .	72
7.6	Shearing results on Lambda and Genomic DNA for 15 mins, 30 mins, and 1 hour sonication time. . . . .	74
8.1	Scattering parameter, $S_{11}$ of FASA element after usage for different durations. . . . .	76
8.2	Resistance (R), reactance (X) and impedance (Z) of FASA element after usage for different durations. . . . .	78

## Tables

2.1	Comparison of different Shearing Techniques . . . . .	15
6.1	Effect of Duty Cycle and Repetition Rate (slow clock) on the DNA Sample . . . . .	58

# Chapter 1

## Introduction

It is well established that the complete information about development and functioning of a living organism is encoded in its DNA; this has very useful implications. For example, we can assume that every disease or disability occurring in an organism could be directly associated with the sequence of a particular DNA segment of that organism. This also means that a disease could be detected, diagnosed and treated more accurately and efficiently if we have a good understanding of genomic data of living beings. Therefore, all pharmaceutical companies, drug discovery companies, forensic laboratories, and biotechnology researchers are very keen in understanding and determining the genome sequence of different organisms. If we can determine the entire DNA sequence of an organism, we can map all of its characteristics to particular DNA fragment-sequences.

Since it is almost impossible to read the entire genome sequence by current sequencers, one needs to fragment the DNA into small fragments, say of different known sizes. The fragments are read to find the order of nucleotides (base-pairs); the reading process is called DNA sequencing. The small fragments are later joined in proper order to build long fragments with the help of computationally intensive reconstruction algorithms. The algorithms are first simulated in order to reconstruct the long chain of base pairs, a step toward reconstructing the whole DNA. The efficacy and success of sequencing technique is dependent on how random the DNA fragments are [1]. The reconstruction algorithm has higher probability of convergence if the

DNA fragments are of different sizes and fragments having different base-pair orders. To this end, we need an efficient DNA shearing system to make DNA libraries so that one could study and compare the properties of different DNA sequences in different organisms. Although the fragment size is largely decided by the maximum base-pair length reading capability of sequencing instrument, it is also decided by the average length of single gene within the organism of interest.

A typical application of DNA shearing and DNA sequencing could be justified by following example. Suppose a person has got tumor in one of his arms and the other arm is healthy. To diagnose, detect, cure or study the tumor-type, one takes DNA samples from both, tumor-affected arm and the healthy arm. DNA samples from both arms are processed and then sheared to fragment sizes which the current genomic-sequencers can read. In this manner we can find the sequence of base-pairs in both unhealthy and healthy DNA samples and can compare them to find tumor-specific variations in genomes. This can eventually help in clinical diagnosis of different types of tumors, and tumor-specific treatments could be devised. This example is pictorially represented in figure-1.1.

There are many methods which can be used to shear the DNA such as enzymatic digestion [2], nebulization [3], hydroshear [1, 4, 5, 6], and sonication [7]-[28]. Enzymatic digestion is a chemical method of shearing the DNA which can not provide random set of fragments, required to build sequencing-library. In nebulization, the shearing of DNA is achieved through atomization or mistification process. Nebulization can provide random fragments of DNA for sequencing but this method has specific requirement for the volume and concentration of input DNA [1]. Hydroshear can provide size-specific random DNA fragments with minimal DNA damage, suitable for sequencing strategies, but the complete process is time consuming. Soni-

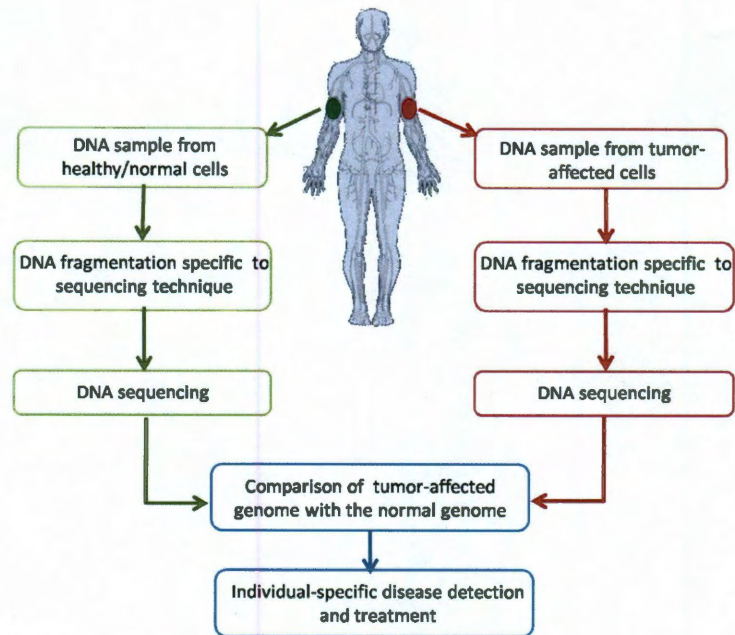


Figure 1.1 : Genome based disease detection and treatment.

cation is among the powerful and controlled methods which can meet the throughput demands of next generation DNA sequencing technologies. Ultrasonic probe, sonoreactor, ultrasonic bath, and adaptive focused acoustic (AFA) are some of the current ultrasound-based platforms for DNA shearing [7, 8].

This thesis describes a fast, efficient, controlled, and scalable DNA shearing system that uses uniquely generated ultrasonic shear forces to shear the DNA to desired fragment sizes. The proposed system uses a specially designed piezoelectric transducer to generate the shear forces. The piezoelectric transducer has sectorized annular electrodes, which generate lateral acoustic waves in the space over it when an RF excitation is applied across the transducer. Such a transducer with sectorized annular electrode pattern is called as Fresnel Annular Sector Actuator (FASA) and has been

successfully used for contactless mixing and thawing of low-volume (1 $\mu$ L-1mL) liquid samples by Microsonic Systems [29, 30, 31]. We modified the existing FASA element and arranged those FASA elements in a particular pattern to generate strong shear forces and used it to shear the DNA samples [32, 33, 34].

The thesis is organized as follows. In chapter-2, we discuss the structure of a DNA molecule and its different representations. Then we discuss the different methods used in practice to shear the DNA. We highlight the advantages and disadvantages of each DNA shearing technique in this chapter. Finally, we compare different DNA shearing techniques with respect to different parameters, namely, the physics behind each technique, the time each technique requires to shear the DNA, the fragment sizes that could be obtained from each technique, the approximate coefficient of variation (CV) of the size of DNA fragments around the mean fragment size, as measured using the Agilent Bioanalyzer 2100, the volume of DNA sample that can be sheared at a time using each technique, the DNA-concentration requirements for each technique, and the approximate cost of the DNA shear system implemented based on each technique. Some of the numbers are approximate in this table. For example, the coefficient of variation of the DNA fragments obtained using different shearing technique varies a lot from one experiment to another. Also, the Bioanalyzer tool can not measure the coefficient of variation very accurately. Finally, the value of coefficient of variation of DNA fragments in a DNA sample changes with the change in the region of interest decided by selecting the position of lower and upper marker in Bioanalyzer plot. Chapter-3 presents the theory and modeling of piezoelectric effect and the common materials exhibiting piezoelectric behavior. This chapter presents a model of piezoelectric rectangular slab excited in its thickness mode. The model computes forces developed at the top and bottom surface of the slab as a function of particle dis-

placement/velocity at top and bottom surfaces of the slab. Finally, the Mason model representing the conversion of electrical energy into acoustic energy and vice-versa is discussed in this chapter. In chapter-4, we present the acoustic field computation due to different shapes of the piezoelectric transducers. This chapter describes the analytical model that we have developed to compute particle displacement due to a transducer. The model could be used to simulate the acoustic field due to flat, also called piston, transducers. We simulate the acoustic potential and particle displacement due to following piezoelectric shapes: circular disc, 360° (full) concentric rings, 270° (sectored) concentric rings, 180° sectored concentric rings, and 90° sectored concentric rings (also called Fresnel Annular Sectored Actuator, FASA). This chapter compares the acoustic quantities (mainly particle displacement) due to different types of piezoelectric transducer. Finally, this chapter presents the simulation based analysis of the proposed circular array-topology of 90° sectored transducers. Chapter-5 describes the fabrication and characterization techniques used for the FASA elements. As a part of characterization, frequency dependent impedance plots and the  $s_{11}$  scattering plots are plotted for each transducer used to shear the DNA. These plots are used to choose the operating frequency and to find the values of lumped components of electrical circuit used to excite the transducer. In chapter-6, we present the architecture of complete DNA shearing system as proposed and implemented in this work. The complete system is divided in to different physical domains- namely, electrical, piezoelectric, and acoustic-fluid interaction domain, based on the physics involved in that domain. In the electrical domain, the digital, analog and RF circuits required to excite the transducer is discusses. While in the piezoelectric and acoustic-fluid interaction domains, the use of piezoelectric material to generate acoustic waves and the interaction of acoustic waves with DNA sample is discussed. Chapter-7 presents the

shearing results of selected experiments performed on real DNA samples. This chapter describes the basic constituents/parameters of shearing protocol and the effect of each parameter on the DNA shearing results in our system. Finally, we summarize the work done in thesis in chapter-8 and discuss the future work required to make the proposed DNA shearing system more robust and reliable.



## Chapter 2

### DNA Shearing

#### 2.1 DNA Structure

DNA is a double helix structure in which each strand consists of two long polymers of simple units, called nucleotides, as shown in figure-2.1 [35]. A nucleotide is made of sugar/phosphate backbone and one of four bases, Adenine (A), Cytosine, (C), Guanine (G) and Thymine (T). The two strands of double helix DNA run in opposite direction and a base of one strand pairs only with its complementary base on the other strand, e.g. adenine always pairs with thymine and guanine pairs with cytosine. DNA is made of millions of base-pairs connected in a particular sequence and a segment of DNA is made of few hundreds to few thousand base-pairs. Figure-2.1 shows segments of DNA in three different ways. Figure-2.1 (a) shows a DNA segment of four base-pairs along with the phosphate backbone on each side [35]. Figure-2.1 (b) shows the double helix form of DNA [36]; at room temperature, the two strands of DNA coils around each other and make a helix structure. Such a DNA is also termed as double-stranded DNA (dsDNA). At elevated temperatures, usually higher than 90°C, the two strands separate and such a DNA is called single-stranded DNA (ssDNA). DNA fragments are also called genes and they contain the genetic information responsible for the development and functionality inside a living organism. If we can determine the entire DNA sequence for an organism, we can map all its characteristics to particular DNA fragment-sequences.

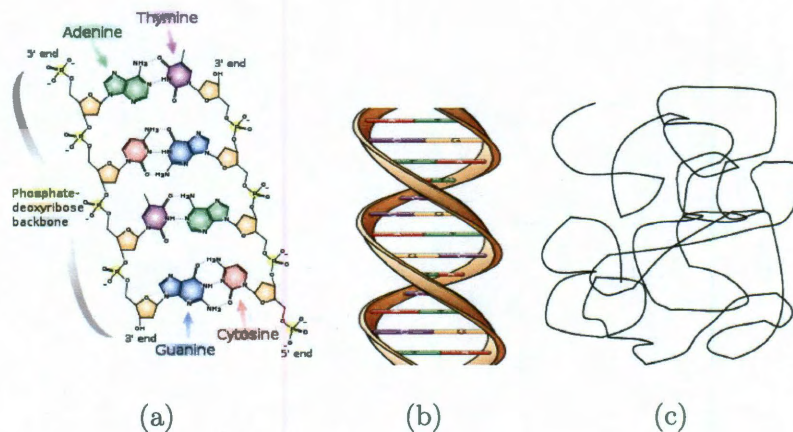


Figure 2.1 : Different representations of DNA molecule: (a) chemical structure of DNA [35] (b) double-helix structure of DNA [36] (c) long entangled DNA.

## 2.2 DNA Shearing Methods

DNA is made of long chain of base-pairs (typically millions) connected in a particular sequence. The DNA is similar to a spaghetti and it is very difficult to read the base-pair sequence for the large DNA. To facilitate DNA sequencer in reading the sequence, the DNA has to be broken into small fragments. Figure-2.2 presents a pictorial representation of DNA before and after shearing. Random shotgun sequencing is the most common method used to determine the sequence of a genome. The success and efficiency of sequencing is dependent on randomness and unbiased cloning of DNA fragments used to build a shotgun library. An ideal library would provide uniform, unbiased coverage, yield a sufficient number of clones for sequence overlap, and have no background of clones without inserts. DNA could be sheared using different methods [37]; some of the common DNA shearing methods are described below.

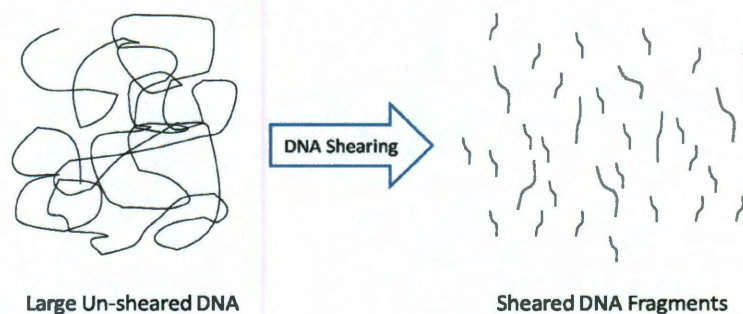


Figure 2.2 : Unsheared DNA and sheared DNA fragments

### 2.2.1 Related Work

1. **Enzymatic DNA Shearing:** There are two types of enzymatic treatments that can be used to shear the DNA- restriction endonuclease and DNase I. Restriction endonuclease partially digests the DNA at fixed sites and hence is used to obtain fragments of fixed sizes. DNase I is another enzyme which in presence of manganese ions result in shearing of DNA. Since these are chemical methods, they are highly concentration-dependent. In addition, these methods are not used for generating fragments targeted for sequencing application because sequencing requires clones of random fragments. Further, these chemical methods not only require the addition of specific enzymes to input DNA but also require the optimization of pH and ionic strength conditions for successful shearing. Also, the addition of extra reagents makes it necessary to purify the DNA after digestion/shearing process and the extra purification step always causes a loss of valuable DNA sample. The enzyme based DNA shearing typically takes 8-10 hours.

Recently, New England BioLabs has announced a better technique of DNA

shearing using their special enzyme-solution and protocols [2]. Their enzyme-solution is named as NEBNext dsDNA Fragmentase and it yields DNA fragments between 100 to 800 bp lengths depending on the reaction time. The solution contains two enzymes, one generates nicks on one of the strands of dsDNA at random sites and the other enzyme recognizes the nicked site and cuts the opposite DNA strand across from the nick, producing dsDNA breaks. The typical reaction time or shearing time is 30 minutes and the results show that NEBNext dsDNA Fragmentase gives better shearing than nebulization and hydroshearing, shearing techniques explained next.

2. **Nebulization Based DNA Shearing:** In this method, DNA sample is placed in a high-pressure chamber, which converts the DNA sample into mist. The mist generated in such manner comes out of an opening and is collected in the container [38]. The final size of DNA fragments is dependent on the applied pressure and is not decided by time. However, the volume of the DNA sample affects the shearing time; higher volume takes more time to nebulize. Higher pressure gives smaller DNA fragments and smaller pressure provides longer fragments. Earlier, when sonication based shearing techniques were not studied fully, it was considered that nebulization was better than sonication, because the latter tended to break DNA at AT-rich regions [37]. This nebulization based shearing is quite cumbersome method and is not scalable to achieve higher throughput, needed to meet the demands of next generation sequencing techniques. Also, the smallest DNA fragment size obtainable using this technique is 700 bp, which is larger than most of the current DNA sequencers. The coefficient of variation of DNA fragments obtained using this technique is also large.

3. **Hydroshear Based DNA Shearing:** In this method the input DNA is passed through a fine-gauge needle whose orifice-diameter and speed of passage decide the size of DNA-fragments. This is one of the simplest methods to shear the DNA but one can not achieve all fragment sizes using this method. The efficiency of this method is highly dependent on the DNA concentration where DNA solutions with higher concentrations can be sheared to smaller sizes than DNA solutions with higher concentrations [1].

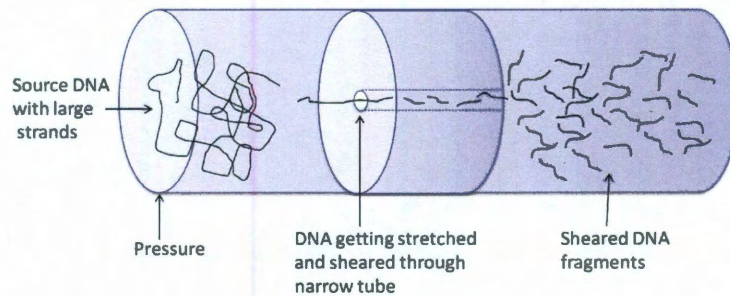


Figure 2.3 : Hydroshear System

4. **Sonication Based DNA Shearing:** This method uses different variations of sound or ultrasonic waves to process the DNA sample and shear it to desired length. Ultrasound is described as high frequency acoustic waves (20 kHz or higher) requiring a medium in order to propagate. There are various shearing platforms which uses sound energy to shear the DNA; some of these are mentioned below.

(a) *Ultrasonic Probe (UP):* Ultrasonic Probe uses small tips which are inserted in DNA sample and they are vibrated at ultrasonic frequency [7]. The UP could achieve DNA fragmentation but this methods has some inherent

disadvantages. Some of the disadvantages are as following: risk of cross-contamination as the tips make direct contact with the DNA sample, loss of sample due to aerosol formation during ultrasonication, thermal degradation of DNA due to rise in temperature from high ultrasonic energy, and potential contamination due to micro-degradation of metallic probe-tips. All these reasons may cause problems during downstream processing of DNA sample.

- (b) *Sonoreactor*: Sonoreactor does not make direct contact with the DNA sample and hence eliminates the contamination and sample loss problems of Ultrasonic Probe [7]. As compared to Ultrasonic Probe, Sonoreactor inputs 50 times less energy than into the sample and hence reduces the temperature-induced thermal degradation problem of UP method. But the size-distribution of DNA fragments obtained using this method is quite broad and lot of sample goes waste during the DNA selection process.
- (c) *Ultrasonic Bath*: In this method, sound energy is generated over large area using array of ultrasonic transducers or one large piezoelectric transducer [7]. This method could shear large amount of DNA at a time but that is not the demand in market. One more problem with this method is that the size-dispersion of DNA fragments is broad which causes higher sample loss in the downstream selection process.
- (d) *Adaptive Focused Acoustic*: Covaris is one of the leading companies which has successfully built a stable DNA shearing system that can give reproducible results [39]. Their technology is based on adaptive focused acoustics (AFA), in which the ultrasound waves are focused to a point in the liquid sample and a vacuum is created at the focal point. This process is

also called cavitation. When passing through an aqueous solution, acoustic waves cause the formation of microbubbles filled with gas (cavities), hence the name cavitation. Two types of cavitation have been observed: stable cavitation (gas body activation) and inertial cavitation (transient or vaporous). Stable cavitation occurs during low intensities of ultrasound, but inertial cavitation requires high intensities of ultrasound. The latter is responsible for high energy events, and considered to be destructive to biological molecules. During inertial sonication, the size of microbubbles varies: first, there is a rapid increase in size, followed by a decrease, until it implodes. The high temperatures and high pressure inside the bubble are sufficient to cause hydrolysis, sonoluminescence phenomena and shearing of biological molecules. Besides cavitation, two additional phenomena may lead to the damage of biological molecules: mechanical and thermal degradation, and reaction with radicals generated from water. Also, the use of ultrasonic waves directly in cells was shown to induce DNA fragmentation and damage. Covaris Inc. has built a DNA shearing system that can shear DNA to fragment sizes between 100 bp (base-pairs) to 5Kbp. The sheared DNA has tight distribution around the targeted mean fragment size, but the time required for the complete process is in the order of hours. Also, their system only processes one sample at a time, so throughput is also one of the problems with their system. Some other methods of shearing DNA are autoclaving/boiling, and mini bead beating.

### 2.2.2 Our Research Work

***Lateral Acoustic Shear Waves Generated Using Proposed System:*** We propose a method of shearing the DNA by generating lateral acoustic waves. The lateral shear waves are generated using RF excitation of specially designed ultrasonic transducers. The piezoelectric plate is patterned with electrodes of special shapes and sizes on its top and bottom surface. These electrode regions, when excited with RF signal generate acoustic waves in space over it and generate an interference pattern. By proper design techniques, we can generate different pressure patterns in the space. When a liquid sample, in particular DNA sample, is placed in the space over transducer, the sample experiences very strong differential acoustic pressure. Such a strong differential pressure causes the large molecules to break into smaller molecules. We use this phenomenon to shear large DNA into small DNA fragments as shown in figure-2.4 [32, 33, 34].

Most large-scale sequencing strategies require random fragmentation of the target DNA into smaller pieces. Physical fragmentation methods such as nebulization, hydrodynamic shearing, and sonication are generally preferred over enzymatic methods, because they are more random, more readily controlled, and they result in a collection of overlapping fragments. The comparison of different DNA shearing is summarized in table 2.1.



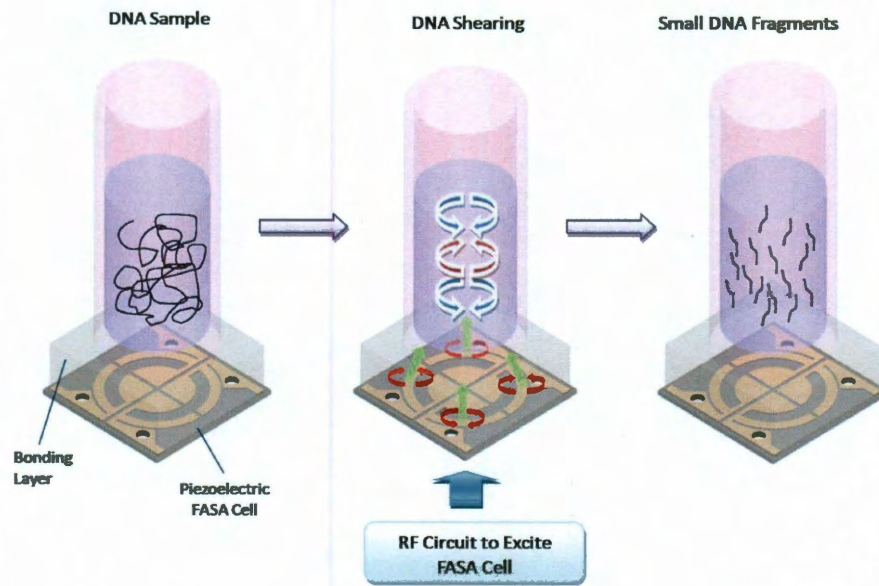


Figure 2.4 : DNA shearing using lateral shear waves

Table 2.1 : Comparison of different Shearing Techniques

	Enzyme Based	Nebulization	Hydroshear	Sonication	
				Covaris	Our System
Physics	Chemical	Atomization	Mechanical	Focused Acoustic	Lateral Waves
Speed	Fast (Minutes)	Fast (Minutes)	Slow (Hours)	Medium Fast (1-4Hours)	Fast (<1Hr)
Fragment Size	Fixed	Random	Specific	Specific	Specific
Volume	Independent -	High 1-2mL	Low > 40μL	Low 100-120μL	Low 50-300μL
Concentration	Independent	High	-	Independent	Independent
Cost	-	Low	Moderate	High	Moderate

## Chapter 3

### Theory and Modeling of Piezoelectric Transducers

#### 3.1 Piezoelectric Effect

Piezoelectric effect is the property of some materials to generate stress/strain in response to applied electric field and also, conversely, to generate electric field in response to applied stress. Hence, theoretically, all piezoelectric materials can be used as transducers, i.e. they can work as both actuators and sensors. The ability to generate electric field or electric potential when a stress is applied to the material is termed as *Direct Piezoelectric Effect*. While the reverse-property of generating stress waves in response to applied electric field is called as *Reverse Piezoelectric Effect*. Some of the examples of piezoelectric materials are as following: lead zirconate titanate ( $Pb[Zr_xTi_{1-x}]O_3, 0 < x < 1$ ), lead titanate ( $PbTiO_3$ ), barium titanate ( $BaTiO_3$ ), barium sodium niobate, lithium niobate, lithium tantalate, quartz, rochelle salt, bismuth germanate, cadmium sulfide, gallium arsenide, tellurium dioxide, zinc oxide, zinc sulfide, ammonium dihydrogen phosphate, aluminum nitride and different chemical variations of these ceramics. For example, lead zirconate titanate, also known as PZT, has different variations: PZT-2, PZT-4, PZT-4D, PZT-5A, PZT-5H, PZT-5J, PZT-7A, and PZT-8. As of today, PZT is the most commonly used piezoelectric material because of its superior properties. We procured PZT transducers from different companies and evaluated them for their performance, reliability, center frequency, and electromechanical conversion efficiency. Eventually, we decided to use the transducers

from Piezo Systems Inc. due to their good value for price [40].

### 3.2 One-dimensional Model of a Piezoelectric Slab Excited in its Thickness Mode

Let us consider a piezoelectric slab in  $x$ - $y$  plane bounded by two planes,  $z = z_1$  and  $z = z_2$ , in  $z$ -direction. The thickness of the slab ( $d = z_2 - z_1$ ) is very small as compared to its length and width. Let us also assume that the piezoelectric material is excited by an RF signal with resonance frequency corresponding to its thickness mode, also called thickness-excitation (TE) mode. Acoustic waves travelling in  $z$ -direction will be generated and these waves will experience reflections from both top and bottom boundaries of piezoelectric slab. A diagram representing such waves is presented in figure-3.1.

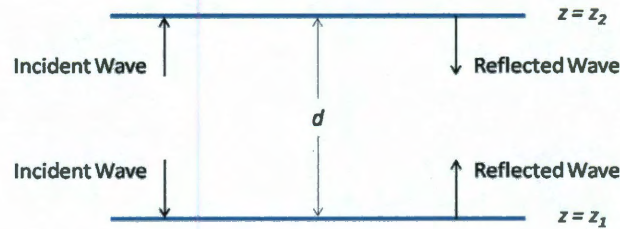


Figure 3.1 : An acoustic medium of finite thickness,  $d$ , with waves propagating in  $+z$  and  $-z$  directions.

We can assume that there are two waves being present in the slab at a time, one wave travelling upward ( $+z$ ) and the other travelling downwards ( $-z$ ). The particle displacement,  $u$  in the piezoelectric medium can then be expressed as

$$u = ae^{-jkz} + be^{jkz} \quad (3.1)$$

Where, the value of coefficients,  $a$  and  $b$ , depends on the acoustic impedance mismatch at two boundaries and  $k$  is the wave vector, equal to  $2\pi/\lambda$ ,  $\lambda$  being the wavelength of acoustic wave inside the slab. Let us assume the particle-displacement to be a simple harmonic function of time ( $ue^{j\omega t}$ , with  $\omega$  being the angular frequency of excitation). The particle velocities at lower and upper boundaries ( $v_1$  and  $v_2$  respectively) are given by

$$v_1 = \left. \frac{du}{dt} \right|_{z=z_1} = j\omega (ae^{-jkz_1} + be^{jkz_1}) \quad (3.2)$$

$$v_2 = \left. \frac{du}{dt} \right|_{z=z_2} = j\omega (ae^{-jkz_2} + be^{jkz_2}) \quad (3.3)$$

From equations (3.2) and (3.3) we can calculate the value of constants  $a$  and  $b$  in terms of  $v_1$  and  $v_2$ . Their values are given by equations (3.4) and (3.5) below.

$$a = -\frac{v_1 e^{jkz_2} - v_2 e^{jkz_1}}{2\omega \sin(kd)} \quad (3.4)$$

$$b = -\frac{v_2 e^{-jkz_1} - v_1 e^{-jkz_2}}{2\omega \sin(kd)} \quad (3.5)$$

Where,  $d$  is the thickness of piezoelectric slab under consideration, i.e.,  $d = z_2 - z_1$ . The analysis presented till now is applicable for any solid material. For a piezoelectric material, the stress ( $T$ ) is related to strain ( $S$ ) and electric field ( $E$ ) as follows [41, 42].

$$T = c^E S - eE = c^E \frac{du}{dz} - eE \quad (3.6)$$

Where,  $c^E$  is the stiffness constant measured at constant  $E$  and  $e$  is the piezoelectric coefficient for the slab. This is one of the fundamental constituent equations of a piezoelectric material. Since piezoelectric slab is typically a dielectric with very

high resistance, the free charge density can be assumed to be zero inside the slab. From Gauss's law, we have  $\nabla \cdot D = \rho_e = 0$ , which implies that the displacement vector inside the piezoelectric slab is constant or zero. In our 1-D example,  $D$  is in  $z$ -direction. Again, for a piezoelectric slab, we have following fundamental equation always being satisfied [41].

$$D = eS + \epsilon^S E = e \frac{du}{dz} + \epsilon^S E \quad (3.7)$$

Where,  $\epsilon^S$  is the dielectric constant (including polarization effect) for the piezoelectric slab. This is the second fundamental constituent equation for a piezoelectric material. From above two equations, (3.6) and (3.7), we get

$$\begin{aligned} T &= c^E \frac{du}{dz} - \frac{e}{\epsilon^S} \left( D - e \frac{du}{dz} \right) \\ &= \left( c^E + \frac{e^2}{\epsilon^S} \right) \frac{du}{dz} - \frac{eD}{\epsilon^S} \\ &= c^D \frac{du}{dz} - \frac{eD}{\epsilon^S} = c^D S - \frac{eD}{\epsilon^S} \end{aligned} \quad (3.8)$$

Where,  $c^D = c^E + \frac{e^2}{\epsilon^S}$  is a new constant. For our one-dimensional case, we can derive the formula for strain by differentiating particle displacement with respect to excitation direction,  $z$ , as following.

$$S = \frac{\partial u}{\partial z} = -jkae^{-jkz} + jkbe^{jkz} \quad (3.9)$$

By substituting the values of  $a$  and  $b$  as derived above, we get following equation for strain ( $S$ ), at all points in a plane at height  $z$ , inside the slab of thickness  $d$ . The slab is bounded by two planes,  $z = z_1$  and  $z = z_2$ , in  $z$ -direction.

$$S = \frac{\partial u}{\partial z} = -jk \left( -\frac{v_1 e^{jkz_2} - v_2 e^{jkz_1}}{2\omega \sin(kd)} \right) e^{-jkz} + jk - \frac{v_2 e^{-jkz_1} - v_1 e^{-jkz_2}}{2\omega \sin(kd)} e^{jkz} \quad (3.10)$$

Substituting the value of  $S$  from equation (3.10) in equation (3.8), we get following identity for stress ( $T$ ).

$$\begin{aligned} T &= c^D \frac{du}{dz} - \frac{eD}{\epsilon^S} \\ &= c^D \left\{ -jk \left( -\frac{v_1 e^{jkz_2} - v_2 e^{jkz_1}}{2\omega \sin(kd)} \right) e^{-jkz} + jk \left( -\frac{v_2 e^{-jkz_1} - v_1 e^{-jkz_2}}{2\omega \sin(kd)} \right) e^{jkz} \right\} - \frac{eD}{\epsilon^S} \end{aligned} \quad (3.11)$$

Let  $T_1$  be the stress generated at bottom surface (at  $z = z_1$ ) and  $T_2$  be the stress at top surface (at  $z = z_2$ ) of piezoelectric slab, the corresponding forces at bottom and top surfaces are given by  $F_1$  and  $F_2$  respectively. We can write

$$\begin{aligned} F_1 &= T_1 A \\ &= \left( c^D \left\{ -jk \left( -\frac{v_1 e^{jkz_2} - v_2 e^{jkz_1}}{2\omega \sin(kd)} \right) e^{-jkz_1} + jk \left( -\frac{v_2 e^{-jkz_1} - v_1 e^{-jkz_2}}{2\omega \sin(kd)} \right) e^{jkz_1} \right\} - \frac{eD}{\epsilon^S} \right) A \\ &= jkc^D A \left( \frac{v_1 e^{jkd} + v_1 e^{-jkd} - 2v_2}{2\omega \sin(kd)} \right) - \frac{eD}{\epsilon^S} A \\ &= j \frac{kc^D A}{\omega} \left( \frac{v_1}{\tan(kd)} - \frac{v_2}{\sin(kd)} \right) - \frac{eD}{\epsilon^S} A \end{aligned} \quad (3.12)$$

Acoustic impedance per unit area is given by the ratio of stress to particle velocity, the total acoustic impedance,  $Z$ , inside the slab with cross-section area  $A$  could be written as:

$$Z = -\frac{T}{\nu} A = \sqrt{\rho c^D} A = \rho \nu_a A = \frac{kc^D}{\omega} A \quad (3.13)$$

Where,  $T$  represents the stress,  $\nu$  is the particle velocity,  $\rho$  is the density of slab,  $\nu_a$  is the phase velocity, and  $c^D$  is a constant dependent on stiffness constant of the piezoelectric slab. The minus sign is used because stress is  $180^\circ$  out of phase with particle velocity. The particle velocity is  $90^\circ$  out of phase with respect to particle displacement. Also, using the following trigonometric identity:

$$\frac{1}{\tan(kd)} = \frac{1}{\sin(kd)} - \tan\left(\frac{kd}{2}\right) \quad (3.14)$$

The equation (3.12) could be re-written as:

$$F_1 = \frac{jZ}{\sin(kd)} (v_1 - v_2) - jZ \tan\left(\frac{kd}{2}\right) v_1 - \frac{eD}{\epsilon^S} A \quad (3.15)$$

Similarly, we can derive an equation for force  $F_2$  at the top surface of the piezoelectric slab.

$$\begin{aligned} F_2 &= T_2 A \\ &= \left( c^D \left\{ -jk \left( -\frac{v_1 e^{jkz_2} - v_2 e^{jkz_1}}{2\omega \sin(kd)} \right) e^{-jkz_2} + jk \left( -\frac{v_2 e^{-jkz_1} - v_1 e^{-jkz_2}}{2\omega \sin(kd)} \right) e^{jkz_2} \right\} - \frac{eD}{\epsilon^S} \right) A \\ &= jkc^D A \left( \frac{2v_1 - v_2 (e^{jkd} + e^{-jkd})}{2\omega \sin(kd)} \right) - \frac{eD}{\epsilon^S} A \\ &= j \frac{kc^D A}{\omega} \left( \frac{v_1}{\sin(kd)} - \frac{v_2}{\tan(kd)} \right) - \frac{eD}{\epsilon^S} A \\ &= \frac{jZ}{\sin(kd)} (v_1 - v_2) + jZ \tan\left(\frac{kd}{2}\right) v_2 - \frac{eD}{\epsilon^S} A \end{aligned} \quad (3.16)$$

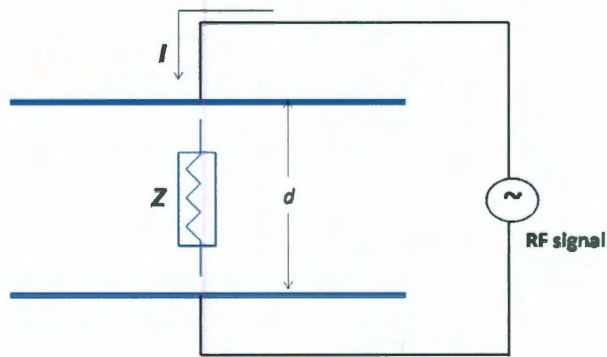


Figure 3.2 : Electrical excitation of piezoelectric slab in thickness mode.

In order to make an equivalent electrical model for the piezoelectric slab, as shown in figure-3.2, we would like to obtain current-voltage characteristic for the slab. Since most of the piezoelectric materials are dielectric, the current through them is purely displacement current. If  $A$  is the area of cross-section of piezoelectric slab through which the current flows, the current density inside slab is given by:

$$\begin{aligned} J &= \frac{\partial D}{\partial t} = j\omega D \\ I &= j\omega DA \end{aligned} \quad (3.17)$$

In the case of direct piezoelectric effect, the voltage developed between the top and bottom surface of the piezoelectric slab could be found by integrating the electric field in  $z$ -direction

$$V = \int_{z_1}^{z_2} E \cdot dz = \int_{z_1}^{z_2} \left( \frac{D}{\epsilon^S} - \frac{e}{\epsilon^S} \frac{\partial u}{\partial z} \right) dz = \frac{Dd}{\epsilon^S} - \frac{e}{\epsilon^S} \{u(z_2) - u(z_1)\} \quad (3.18)$$

Where,  $d = z_2 - z_1$ . Since displacement current  $D = \frac{I}{j\omega A}$ , and particle velocity,  $v = \frac{\partial u}{\partial t} = j\omega u$ , we arrive at following equation:

$$\begin{aligned} V &= \frac{d}{\epsilon^S} \frac{I}{j\omega A} - \frac{e}{\epsilon^S} \left( \frac{v_2 - v_1}{j\omega} \right) \\ \Rightarrow I &= j\omega \frac{\epsilon^S A}{d} V - \frac{e}{\epsilon^S} \frac{\epsilon^S A}{d} (v_1 - v_2) \end{aligned} \quad (3.19)$$

By substituting  $h = \frac{e}{\epsilon^S}$  and  $C_0 = \frac{\epsilon^S A}{d}$ , we get following current-voltage ( $I - V$ ) relationship inside the piezoelectric slab.

$$I = j\omega C_0 V - hC_0 (v_1 - v_2) \quad (3.20)$$



Here  $C_0$  can be considered as the static electrical capacitance at zero or fixed strain. From the above  $I - V$  equation, we notice that the current flowing through piezoelectric slab is composed of two terms: 1) the displacement current through a capacitance,  $j\omega C_0 V$ ; and, 2) the current due to conversion of mechanical energy to electrical polarization due to piezoelectric effect,  $hC_0(v_1 - v_2)$ . Hence, this equation relates electric current to acoustic current and it is a very important relationship.

When we substitute values of  $D$  and  $h$  in the equations for forces at two surfaces, we get following equations for  $F_1$  and  $F_2$ .

$$F_1 = \frac{jZ}{\sin(kd)} (v_1 - v_2) - jZ \tan\left(\frac{kd}{2}\right) v_1 - \frac{h}{j\omega} I \quad (3.21)$$

$$F_2 = \frac{jZ}{\sin(kd)} (v_1 - v_2) + jZ \tan\left(\frac{kd}{2}\right) v_2 - \frac{h}{j\omega} I \quad (3.22)$$

Now, we can build an equivalent circuit of a piezoelectric slab as shown in figure-3.3. This model is widely known as Mason model, after Warren Mason, who performed a lot of pioneer work in crystal acoustics [41]. In Mason's model, force in acoustic domain is analogous to voltage in electrical domain and velocity in acoustic domain is equivalent to current in electrical domain.

In figure-3.3, an electrical current flows in left-side, i.e. terminals a-b, of the transformer and an acoustic current  $(v_1 - v_2)$  flows in the right side of the transformer. Hence, the transformer in the Mason's circuit represents the conversion of electrical energy to acoustic energy and vice-versa. We can assume the equations derived for forces at top and bottom surfaces of slab,  $F_2$  and  $F_1$  respectively, for acoustic domain to be equivalent to Kirchhoff's voltage laws in electrical domain. Hence, we find that the voltage at terminal c-d is given by

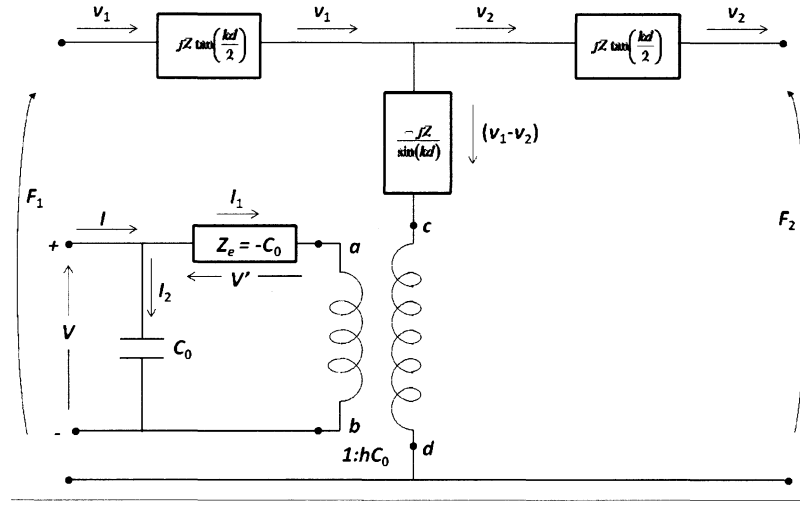


Figure 3.3 : Mason model equivalent circuit of a finite thickness piezoelectric plate

$$V_{cd} = \frac{h}{j\omega} I \quad (3.23)$$

Since the turn-ratio between right side to left side windings of the transformer is equal to  $hC_0$ , we have following voltage at terminal a-b

$$V_{ab} = \frac{I}{j\omega C_0} \quad (3.24)$$

Writing Kirchhoff's voltage law at left side of the transformer circuit, we get

$$\begin{aligned} V' &= V - v_{ab} = \frac{I_2}{j\omega C_0} - \frac{I}{j\omega C_0} \\ &= -\frac{I_1}{j\omega C_0} \text{ (Since } I = I_1 + I_2 \text{)} \\ \Rightarrow V' &= \frac{jI_1}{\omega C_0} \end{aligned} \quad (3.25)$$

As we can see in figure-3.3,  $V'$  is the voltage across impedance  $Z_e$  and it is equal to  $\frac{j}{\omega C_0}$ , assuming that  $I_1$  is the current flowing away from the node. We immediately

notice that the impedance  $Z_e$  is of a unique kind- it behaves like a negative capacitor. That is, the impedance is like a capacitor because its reactance varies inversely with frequency, but it is also like an inductor because the magnitude of its reactance is positive. This does not necessarily mean that there exists a passive element whose impedance has properties similar to  $Z_e$ ; it just helps in making the theoretical model complete.

The Mason's model needs to be modified to include the effect of electrodes, typically made of different materials, which are patterned on top and bottom surfaces of piezoelectric slab. In practical acoustic applications, e.g. in the mixing application or in our DNA shearing application, water is used as coupling medium between the transducer and target (in our case, the target is nothing but the container holding the sample).

## Chapter 4

### Acoustic Field Due to Different Piezoelectric Transducers: Simulation Based Analysis

It was shown in chapter-3 that acoustic pressure-waves are generated from a piezoelectric plate when a time varying voltage signal is applied across it. We made an assumption that the particle displacement inside piezoelectric material is  $u$ , after considering the superimposition of two types of waves travelling in opposite directions inside the piezoelectric material. Based on that assumption, we derived the model equations for the piezoelectric slab. Such waves are generated inside piezoelectric materials when an RF signal is applied across it. The stress waves associated with the particle displacement are not just contained inside the transducer, these waves also propagate in all directions in space around the transducer. One could characterize this transduction process, i.e. the amount of stress waves generated in response to different voltages applied across the transducer could be characterized. Hydrophone is an example of such device that is used to measure the intensity of vibrations inside liquid and is typically used to characterize different piezoelectric transducers. For acoustic simulations presented in this chapter, we have assumed that the particle displacement just at the surface of the slab is known, and it is denoted as  $u_0$ . Also, we assume that the particle displacement at the surface of slab is a wave function having temporal behavior similar to the RF signal applied across the transducer.

In this thesis, we have analyzed only planar geometries of the piezoelectric transducers, also called piston transducers, because they are easy to fabricate and the

fabrication process is compatible to MEMS fabrication process. In reality, a transducer could be manufactured of any shape/geometry depending on the application it is used for. For example parabolic-shaped transducers are sometimes used in applications requiring acoustic focusing. The pressure/stress waves generated from a transducer travel as spherical waves in the space over the slab. We want to compute the particle displacement at any point in space due to the stress-waves generated inside the piezoelectric slab.

#### **4.1 Plane/Flat Piston Transducers With Different Electrode Patterns**

The plate transducers, also called piston transducers, have planar geometry. For thickness excitation of these transducers, an RF signal is applied in thickness direction, i.e. between top and bottom electrode of the transducer. The slab is assumed to be larger by many magnitudes in other two dimensions than in thickness direction. One can use different shapes of electrodes to excite a piezoelectric slab. Figure- 4.1 shows some of the shapes of electrodes that we will analyze in this thesis. Piezoelectric slab is sandwiched between top and bottom electrodes to generate stress field in space. In figure-4.1(a), layers of circular electrodes are deposited on both surfaces of a rectangular piezoelectric slab; the green region represents the piezoelectric slab and the blue region corresponds to the electrode. In the figure, we see only top electrode, although there is similar electrode patterned on the bottom side of the slab also. Usually, the size of piezoelectric slab is larger than the electrodes' area. Here, only the circular region of piezoelectric slab generates acoustic field which lie exactly between the circular electrodes. The electrodes are typically made of high-conductivity

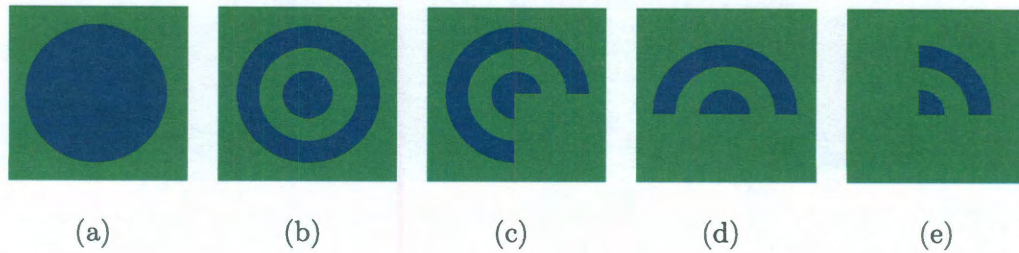


Figure 4.1 : Electrodes (in blue color) of different shapes patterned on piezoelectric square block (in green color): (a) circular plate electrode (b) full-ring electrode (c) 270° FASA element with two rings (d) 180° FASA element with two rings (e) 90° FASA element with two rings.

materials, e.g. Cu, Au, Ag, Pt etc. The thickness of electrode layer is generally a few micrometers ( $1-50 \mu\text{m}$ ), which is far lesser than the thickness of piezoelectric slab ( $0.5-2 \text{ mm}$ ) for operating frequency between 1MHz and 4MHz. The resonant frequency of piezoelectric slab changes with the thickness of slab; hence, thickness of the slab literally decides the operating frequency. Also, for thickness mode excitation of piezoelectric slab, the length and width of piezoelectric slab are significantly larger than its thickness.

It is important to note that stress-waves or acoustic-waves are generated from only those regions of piezoelectric plate/slab which lie precisely between the two electrodes. The regions of piezoelectric slab which are not sandwiched by any electrode, and hence not excited by any signal, do not generate any acoustic wave. The cutoff between active and inactive zone is very sharp for most of the modern piezoelectric materials. Figure-4.1(b) shows a rectangular piezoelectric slab (green slab) with top electrode having two full rings (blue-rings). The bottom surface of piezoelectric slab is also patterned with two rings of similar dimensions so that the top and bottom electrodes lie exactly over one-another. It is worth emphasizing again that in figure-4.1(b) complete rectangular green slab does not generate stress waves; only, the region

which lies between top and bottom electrodes generate stress waves.

Figure-4.1(c), (d) and (e) show Fresnel Annular Sector Actuator of 270°, 180° and 90° sector angles respectively. The waves generated from different points on electrode reach at a point in space with different path lengths; due to path-differences between different acoustic waves, interference pattern will be formed in space. The resultant acoustic field is computed by superimposing the field generated by different points on electrode.

## 4.2 Circular Plate Transducer

In this section, we consider a piezoelectric slab sandwiched between two electrodes of circular shape as shown in figure-4.2. In this figure, blue colored plates at the top and bottom surface represent two electrodes, and green slab in between these electrodes is the piezoelectric plate itself. When an RF signal is applied between two electrodes with RF-frequency corresponding to the thickness resonance of the piezoelectric plate, stress waves are generated inside and outside of the transducer plate. The fundamental frequency of vibration of these stress waves is same as the frequency of RF-excitation. Since complete electrode-area is excited by same voltage, we can assume that the particle displacement right above (i.e.  $z = 0+$ ) the transducer surface is same at every point at a particular instant of time. Let the particle displacement at the transducer surface be  $u_0$ . Since the shape of electrodes are circularly symmetric, we will write all equations and derivations in cylindrical coordinate system. The acoustic potential per unit area at distance  $R$  from a point source of spherical wave is given by [43]:

$$\Phi(r, \psi, z) = -\frac{u_0}{2\pi} \frac{e^{-(\alpha+jk)R}}{R} \quad (4.1)$$

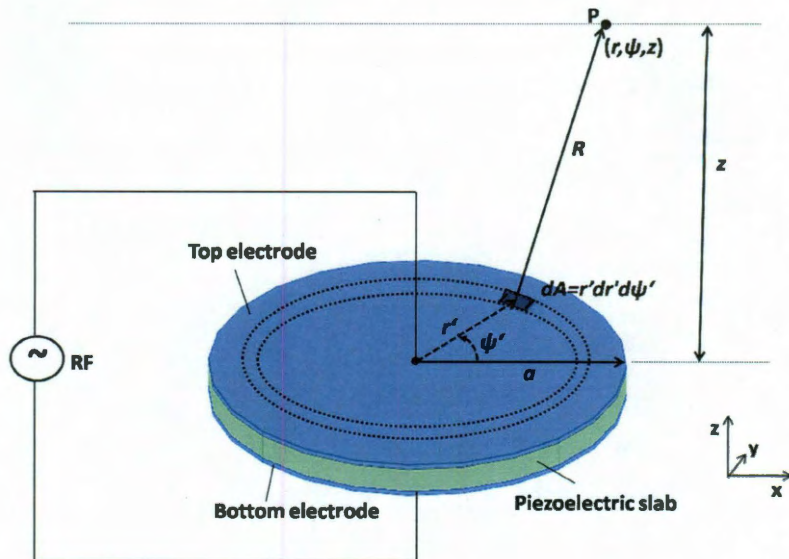


Figure 4.2 : Computation of acoustic field at a point P due to circular piezoelectric slab.

To compute the acoustic potential due to whole circular electrode-area of radius  $a$ , we first consider a small elemental area at a radial distance  $r'$  and angular distance  $\psi'$  on the top circular-electrode [44, 45]. We, then use integration to find the acoustic potential due to complete electrode area. Let the area of a small element is  $dA = r' dr' d\psi'$ ; this differential area element is located at coordinate  $(r', \psi', 0)$  in cylindrical system. The  $z = 0$  plane represents the top electrode on the slab. The acoustic potential ( $\Phi$ ) due to whole circular electrode at point P located at  $(r, \psi, z)$  is given by

$$\Phi(r, \psi, z) = -\frac{u_0}{2\pi} \int_{\psi'=0}^{2\pi} \int_{r'=0}^a \frac{e^{-(\alpha+jk)R}}{R} r' d\psi' dr' \quad (4.2)$$

Where,  $\alpha$  is the acoustic attenuation constant of the medium,  $k$  is the wave vector ( $= 2\pi/\lambda$ ) and  $R$  is the distance between point P and the elemental area  $dA$ . It can



be shown that  $R = \sqrt{z^2 + r^2 + r'^2 - 2rr' \cos(\psi - \psi')}$ .

Once the acoustic potential is known at point P, the relative particle displacement (in radial, vertical, and circumferential directions) can be calculated by differentiating the acoustic potential at that point. That is

$$u = \nabla \Phi(r, \psi, z) = \left( \frac{\partial}{\partial r} \hat{r} + \frac{\partial}{r \partial \psi} \hat{\psi} + \frac{\partial}{\partial z} \hat{z} \right) \Phi(r, \psi, z) \quad (4.3)$$

Hence, relative particle displacement in radial direction ( $u_r$ ) can be written as

$$\begin{aligned} u_r &= \frac{\partial}{\partial r} \Phi(r, \psi, z) |_{\psi=\text{const}, z=\text{const}} = \frac{\partial}{\partial r} \left( -\frac{u_0}{2\pi} \int_{\psi'=0}^{2\pi} \int_{r'=0}^a \frac{e^{-(\alpha+jk)R}}{R} r' d\psi' dr' \right) \\ \Rightarrow u_r &= \frac{u_0}{2\pi} \int_{\psi'=0}^{2\pi} \int_{r'=0}^a \frac{e^{-(\alpha+jk)R}}{R^3} \{1 + (\alpha + jk) R\} \{r - r' \cos(\psi - \psi')\} r' d\psi' dr' \end{aligned} \quad (4.4)$$

Similarly, the circumferential component of relative particle displacement ( $u_\psi$ ) is given by

$$\begin{aligned} u_\psi &= \frac{\partial}{r \partial \psi} \Phi(r, \psi, z) |_{r=\text{const}, z=\text{const}} = \frac{\partial}{r \partial \psi} \left( -\frac{u_0}{2\pi} \int_{\psi'=0}^{2\pi} \int_{r'=0}^a \frac{e^{-(\alpha+jk)R}}{R} r' d\psi' dr' \right) \\ \Rightarrow u_\psi &= \frac{u_0}{2\pi} \int_{\psi'=0}^{2\pi} \int_{r'=0}^a \frac{e^{-(\alpha+jk)R}}{R^3} \{1 + (\alpha + jk) R\} r'^2 \sin(\psi - \psi') d\psi' dr' \end{aligned} \quad (4.5)$$

And, the  $z$ -component of particle displacement ( $u_z$ ) can be computed as

$$\begin{aligned} u_z &= \frac{\partial}{\partial z} \Phi(r, \psi, z) |_{r=\text{const}, \psi=\text{const}} = \frac{\partial}{\partial z} \left( -\frac{u_0}{2\pi} \int_{\psi'=0}^{2\pi} \int_{r'=0}^a \frac{e^{-(\alpha+jk)R}}{R} r' d\psi' dr' \right) \\ \Rightarrow u_z &= \frac{u_0}{2\pi} \int_{\psi'=0}^{2\pi} \int_{r'=0}^a \frac{e^{-(\alpha+jk)R}}{R^3} \{1 + (\alpha + jk) R\} z r' d\psi' dr' \end{aligned} \quad (4.6)$$

We can easily compute the particle displacements in Cartesian coordinate system, or for that matter in any coordinate system, once we have their values in cylindrical

coordinate system, equations (4.4), (4.5), and (4.6). The simulated particle displacements due to a circular electrode of 4mm radius are shown in figure-4.3. The vertical component is given by same equation in both cylindrical and Cartesian coordinate systems. Only the planar components ( $u_x$  and  $u_y$ ) needs to be computed again. It is sometimes required to compute  $u_x$  and  $u_y$  to plot the quiver plot of particle displacement in a plane. The particle displacement in  $x$  and  $y$  directions are given by following equations.

$$u_x = u_r \cos \psi - u_\psi \sin \psi \quad (4.7)$$

$$u_y = u_r \sin \psi + u_\psi \cos \psi \quad (4.8)$$

In equations (4.4), (4.5) and (4.6) for  $u_r$ ,  $u_\psi$  and  $u_z$ , we have assumed that the particle displacement just above the surface of transducer at a particular time instant is  $u_0$ . Typically,  $u_0$  varies with time because piezoelectric transducer is excited by a time varying RF-signal. We denote  $U$  as the particle displacement at any time instant. After computing the particle displacement at point P as a function of time, we can easily compute the particle velocities by differentiating it with respect to time. If the particle displacement  $U$  is a simple harmonic function of time, i.e.,  $U = u \cos(\omega t)$ , we can find the particle velocity as follows:

$$v = \frac{\partial U}{\partial t} = -u\omega \sin(\omega t) \quad (4.9)$$

We can obtain  $x$ ,  $y$  and  $z$  components (or  $r$ ,  $\psi$ , and  $z$  components in cylindrical coordinate system) of particle velocity at point P, or for that matter at every point in space. In fluid mixing applications, the sample to be mixed is placed over the transducer.

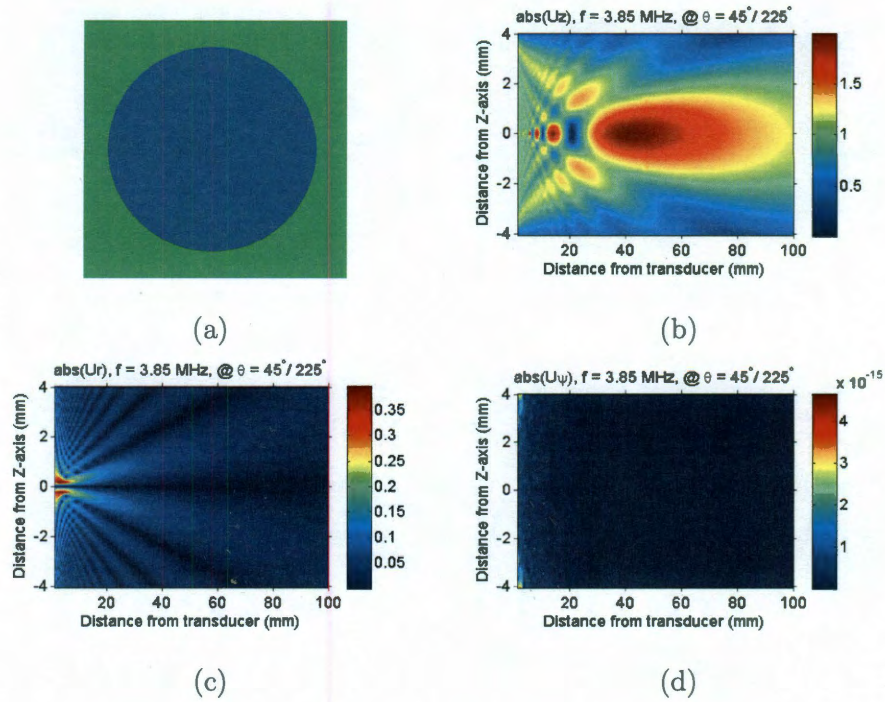


Figure 4.3 : (a) Circular-plate electrode of  $4\text{mm}$  radius; (b) vertical-component of particle displacement ( $u_z$ ); (c) radial-component of particle displacement ( $u_r$ ); (d) circumferential-component of particle displacement ( $u_\psi$ ).

There are two distinct regions of interest, the near-field and far-field regions. The near-field region is also called Fresnel zone and the far-field region is sometimes called Fraunhofer zone. The main difference between these two regions is that the diameter of the acoustic beam emitted from the transducer remains uniform in Fresnel zone and the beam spreads in diameter in the Fraunhofer zone. There is not an abrupt change in the field pattern at the boundary of near-field and far-field though. Also, within Fresnel zone, there are rapid variations of acoustic field in the beam in both vertical/axial and radial directions, while in Fraunhofer zone, the stress fields remain uniform over a large diameter. It is worth mentioning that an ultrasonic

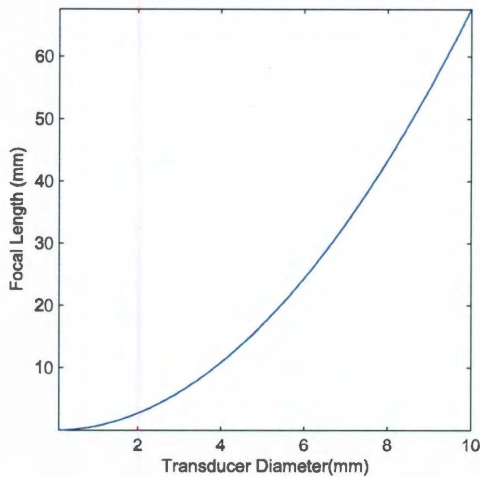


Figure 4.4 : Natural focal length versus diameter of the transducer at 4MHz in water.

transducer with circular electrode has a fixed focal length, and the natural focus is at a distance  $\frac{D^2 * f}{4 * speed}$  from the transducer, where  $f$  is the operating frequency,  $D$  is the transducer diameter and  $speed$  is the speed of sound in the medium. The dependence of transducer diameter on the focal length of a circular transducer is plotted in figure-4.4.

The vertical component of acoustic field is maximum at the boundary of these two regions; this could also be observed from the simulation results plotted in figure 4.3 (b). It requires the sample or object under investigation to be placed at a fixed distance from the transducer [43]. The focal length in this case is dependent only on the diameter of the electrode (the electrodes are kept circular shape due to their circularly symmetric acoustic field).

### 4.3 Plane Transducer With Full-ring Electrode Pattern

In order to better control the focal length of an ultrasonic transducer while allowing the transducer to be of any size, the electrodes on the transducer could be designed in the shape of rings.

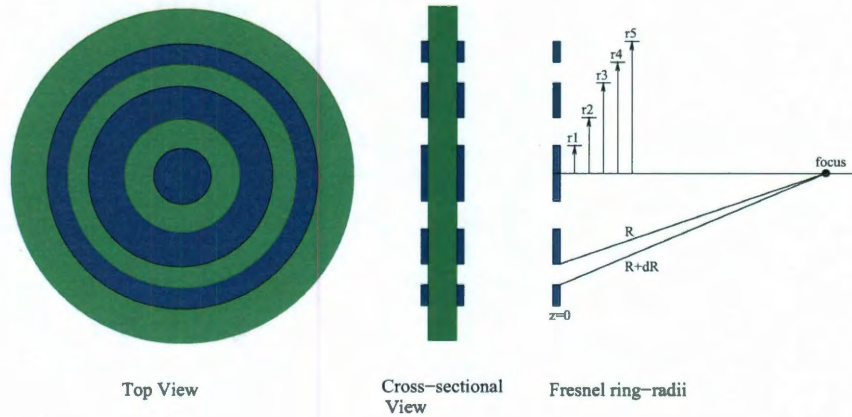


Figure 4.5 : Top view, cross-sectional view and ring-radii of a three-ring Fresnel lens

#### 4.3.1 Acoustic Fresnel Lens

The electrodes on a piezoelectric plate can be patterned in the shape of circular rings of certain widths in order to focus acoustic field at a point in space through constructive interference of waves [46]. To achieve a constructive interference the ring widths and ring radii are chosen such that the path difference between the acoustic waves reaching to focal point from outer side of one ring and inner side of the next larger ring is equal to an integer multiple of  $\lambda/2$ . Such acoustic source is called as a Fresnel half-wave band (FHWB) source. There are two types of FHWB sources—positive wave FHWB and negative-source FHWB [46, 47, 48]. The positive-wave FHWB are those lens that have the innermost ring (first-ring) with non-zero inner

and outer radii; this means that the waves generated from first ring have path-length of at least  $\lambda/2$  higher than the focal-length itself. On the other hand the negative-wave FHWB sources have zero inner radii for the first ring. If the focal length of the transducer is  $F$ , the path-length of waves generated from first ring is between  $F$  and  $F + \lambda/2$ . A negative-source FHWB with three rings is shown in figure-4.5. Let  $F$  be the focal length,  $r_n$  and  $r_{n+1}$  be the inner and outer radii of a ring, and  $dR$  be the path-difference between adjacent rings. Mathematically, we can write it as following.

$$dR = \sqrt{F^2 + r_{n+1}^2} - \sqrt{F^2 + r_n^2} = \frac{\lambda}{2}$$

Where,  $n = 0, 1, 2, 3, \dots$

$$r_0 = 0 \tag{4.10}$$

In other words, one could write the path difference between waves generated from  $N^{th}$  ring and from the center of first ring as  $N$  time half-wavelength. If the indexing is done such that  $r_n$  represents the inner or outer radius of a ring,  $(\lfloor \frac{n}{2} \rfloor + 1)^{th}$  ring, we could write:

$$R_n - F = \sqrt{F^2 + r_n^2} - F = n \frac{\lambda}{2}$$

$$\Rightarrow r_n = \sqrt{\left(F + n \frac{\lambda}{2}\right)^2 - F^2}$$

$$\Rightarrow r_n = \sqrt{\left(n \frac{\lambda}{2}\right)^2 + n\lambda F} \tag{4.11}$$

### 4.3.2 Acoustic Field due to 360° Fresnel Lens

In a typical application, the transducer size to be used is first decided based on the power-level requirement or the space-constraints. For example, in our DNA shearing

product, we want to design the transducer such that it could shear 96 DNA samples at a time placed in a microplate area. The pitch of a standard microplate is 9mm. Therefore, we had to design the transducer within 9mm by 9mm; this also includes the area needed for electrical pads or interconnects required for exciting the transducer. Once the size of the transducer is fixed, the focal length and operating-frequency decide the number of rings in the transducer. The focal length of the transducer is usually decided by the application in which the transducer is used. As mentioned earlier, the operating frequency is decided by the thickness of the transducer. In our application, the average operating frequency of different transducers is 3.85MHz. We designed the transducers for 13mm focal length because at 3.85MHz, we wanted to fit atleast two electrode rings in the 8mm by 8mm area; remaining 1mm space is utilized for electrical pads and routing of RF signal. At focal length more than 13mm, we can not fit two rings in 8mm by 8mm, so, we chose the 13mm focal length for our design and simulations.

Once the focal length, operating frequency and the maximum size of transducer is decided, we can easily find the number of rings that can fit in the area. For two ring negative source Fresnel transducer design, there are three different radii needed to design the rings:  $r_1$ , the radii of first ring;  $r_2$ , the inner radii of second ring; and  $r_3$ , the outer radii of second ring. The inner radius ( $r_0$ ) of the first ring is zero. With these parameters, the acoustic field due to Fresnel ring transducer can be computed by adding the field from each ring. That is, for a two ring 360° transducer, the radial ( $u_r$ ), circumferential ( $u_\psi$ ), and vertical component ( $u_z$ ) of the particle displacement is computed as following:

$$u_r = \frac{u_0}{2\pi} \int_{\psi'=0}^{2\pi} \sum_{i=1}^{n=2} \left[ \int_{r'=r_{2(i-1)}}^{r_{2i-1}} \frac{e^{-(\alpha+jk)R}}{R^3} \{1 + (\alpha + jk) R\} \{r - r' \cos(\psi - \psi')\} r' dr' \right] d\psi' \quad (4.12)$$

$$u_\psi = \frac{u_0}{2\pi} \int_{\psi'=0}^{2\pi} \sum_{i=1}^{n=2} \left[ \int_{r'=r_{2(i-1)}}^{r_{2i-1}} \frac{e^{-(\alpha+jk)R}}{R^3} \{1 + (\alpha + jk) R\} r'^2 \sin(\psi - \psi') dr' \right] d\psi' \quad (4.13)$$

$$u_z = \frac{u_0}{2\pi} \int_{\psi'=0}^{2\pi} \sum_{i=1}^{n=2} \left[ \int_{r'=r_{2(i-1)}}^{r_{2i-1}} \frac{e^{-(\alpha+jk)R}}{R^3} \{1 + (\alpha + jk) R\} zr' dr' \right] d\psi' \quad (4.14)$$

Where,  $i$  is the ring number and  $r_0, r_1, r_2, \dots$  are inner/outer radii of different rings and  $n$  denotes the number of rings in the transducer.

The acoustic field due to two-ring Fresnel lens is shown in figure-4.6. By comparing the plots of figure-4.3 and 4.6, we confirm that the ring-shaped electrode has higher radial and vertical component of particle displacement than that due to the circular transducer even though the total active area is higher in a circular transducer. The circumferential component due to both circular and ring-shaped transducer is negligible. The acoustic field at a fixed distance from complete annular electrodes is symmetrical in the horizontal plane and the field is intensified in vertical direction. Hence the acoustic source in the shape of complete annular electrodes ( $360^\circ$ ) is useful in the liquid ejector applications [48]. Next, we present some transducer designs which have higher rotational component of acoustic particle displacement as well as large radial and vertical component of particle displacement per unit electrode area.



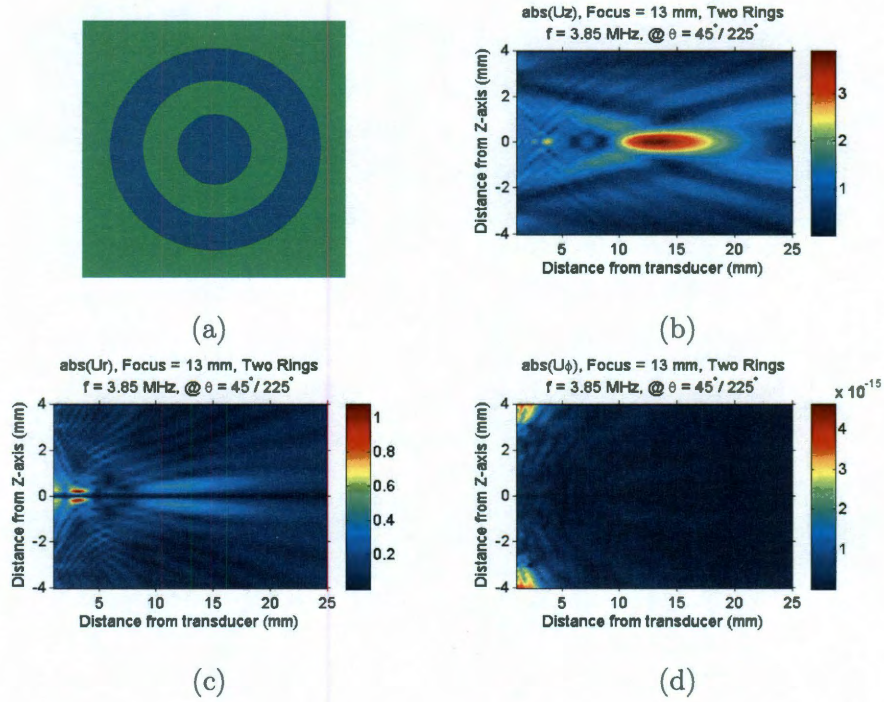


Figure 4.6 : (a) Full ring (360°) electrode with 13mm focal length; (b) vertical-component of particle displacement ( $u_z$ ); (c) radial-component of particle displacement ( $u_r$ ); (d) circumferential-component of particle displacement ( $u_\psi$ ).

#### 4.4 Piezoelectric Transducer with Sectored Annular Electrodes

Since both circular and 360° transducers have circular symmetry, the rotational component of acoustic field is zero. We design non-360° annular transducers to increase the circumferential (responsible for vortexing) component of particle displacement in fluid due to acoustic potential. We present simulation results for three sector-angles other than 360° angle: 90°, 180°, and 270°; these transducers are shown in figure-4.1 (c)-(e). The 90° transducer was first proposed in [29] and it was shown that such a transducer generates rotational field causing the liquid to vortex in opposite direc-

tions. We computed the particle displacements ( $u_r$ ,  $u_\psi$  and  $u_z$ ) due to  $90^\circ$ ,  $180^\circ$ , and  $270^\circ$  transducers. In all cases, the transducers are designed for focal length of 13mm at 3.85MHz and the maximum size of the transducer is limited to 8mm by 8mm; with these design parameters, the transducer can have maximum two-rings that could fit in the constrained area. All sectorized transducers are assumed to be placed around the origin (0,0), as shown in figure-4.1. Next we present the acoustic field due to these sectorized transducers.

#### 4.4.1 $270^\circ$ Sectorized Annular Transducer

A  $270^\circ$  sectorized transducer and its acoustic field in a plane at 13mm away from the transducer is shown in figure-4.7. For a two ring transducer, the radial ( $u_r$ ), circumferential ( $u_\psi$ ), and vertical component ( $u_z$ ) of the particle displacement due to  $270^\circ$  transducer are computed as following:

$$u_r = \frac{u_0}{2\pi} \int_{\psi'=0}^{3\pi/2} \sum_{i=1}^{n=2} \left[ \int_{r'=r_{2(i-1)}}^{r_{2i-1}} \frac{e^{-(\alpha+jk)R}}{R^3} \{1 + (\alpha + jk) R\} \{r - r' \cos(\psi - \psi')\} r' dr' \right] d\psi' \quad (4.15)$$

$$u_\psi = \frac{u_0}{2\pi} \int_{\psi'=0}^{3\pi/2} \sum_{i=1}^{n=2} \left[ \int_{r'=r_{2(i-1)}}^{r_{2i-1}} \frac{e^{-(\alpha+jk)R}}{R^3} \{1 + (\alpha + jk) R\} r'^2 \sin(\psi - \psi') dr' \right] d\psi' \quad (4.16)$$

$$u_z = \frac{u_0}{2\pi} \int_{\psi'=0}^{3\pi/2} \sum_{i=1}^{n=2} \left[ \int_{r'=r_{2(i-1)}}^{r_{2i-1}} \frac{e^{-(\alpha+jk)R}}{R^3} \{1 + (\alpha + jk) R\} z r' dr' \right] d\psi' \quad (4.17)$$

Where,  $i$  is the ring number and  $r_1, r_2, \dots$  are inner/outer radii of different rings and  $n$  denotes the number of rings in the transducer.

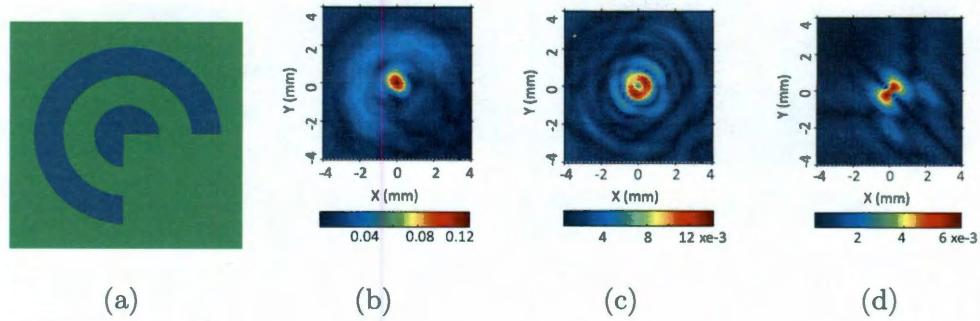


Figure 4.7 : (a) 270° FASA ring electrode with 13mm focal length; (b) vertical-component of particle displacement ( $u_z$ ); (c) radial-component of particle displacement ( $u_r$ ); (d) circumferential-component of particle displacement ( $u_\psi$ ).

From figure-4.7 (b), we notice that the vertical component of particle displacement has its maxima near origin, as in 360° rings case, but the maximum intensity is more spread in 270° case. We would appreciate this later once we discuss the simulation results for other sector-angles; the maximum intensity point of  $u_z$  for 270° transducers are mostly located in the region right above the transducers. So, even though the maxima intensity points look circularly located around the origin in this case, the maxima points are mostly in the first three quadrants for the transducer having active area in first three quadrants.

The radial component of particle displacements ( $u_r$ ) at 13 mm height from a 270° sectored annular transducers is shown in figure-4.7 (c). Typically, the  $u_r$  of a sectored transducer has its maxima in the direction diagonally opposite to the orientation of the transducer. For example, a 270° transducer covering I, II, and III quadrants has the orientation of 135°, so the maximum intensity of  $u_r$  is in the 315° (= 135+185) direction, i.e. in IV quadrant. The  $u_r$  is spread mainly in three quadrants, I, III and IV, and not in II quadrants. The understanding of acoustic patterns due to different sector angles is necessary to choose the right sector-angle for the transducer for an

application. The importance of choosing right-sector angle for the transducer based on its acoustic field will become more clear when we would discuss the phase-array transducer design (section 4.4.4), wherein more than one sector-transducers could be made active or inactive at a particular instant of time.

It is observed from the simulation results that the circumferential component of particle displacement ( $u_\psi$ ) due to sectored transducers has a unique characteristic. The maximum rotational component of a sectored transducer is always in the plane perpendicular to the orientation of the rings of the transducer. This could be seen from the simulation result plotted in figure-4.7 (d). The  $u_\psi$  due to 270° transducers has peaks in the (45°, 225°) direction because the transducer is oriented towards 135°. The (45°, 225°) direction could also be thought of as a line passing through origin and is at 45° from x-axis. More importantly, 270° sectored transducer has higher rotational acoustic field than a full ring transducer, which has zero rotational component (compare figure-4.7 (d) and figure-4.6 (d)). So, 270° transducer is better than a 360° transducer for mixing or fluid processing applications.

#### 4.4.2 180° Sectored Annular Transducer

In this section, we discuss the acoustic field pattern due to a 180° sectored annular piezoelectric transducer. The particle displacements at 13mm height from the transducer due to 180° transducer is shown in the figure-4.8. The radial ( $u_r$ ), circumferential ( $u_\psi$ ), and vertical component ( $u_z$ ) of the particle displacement due to 180° transducer is computed using equations 4.15 -4.17, except that the integral limits for  $\psi'$  is 0 to  $\pi$  instead of 0 to  $3\pi/2$ .

The vertical displacement component has only one prominent maxima at the origin but the acoustic field is spread over two quadrants where the transducer is placed;

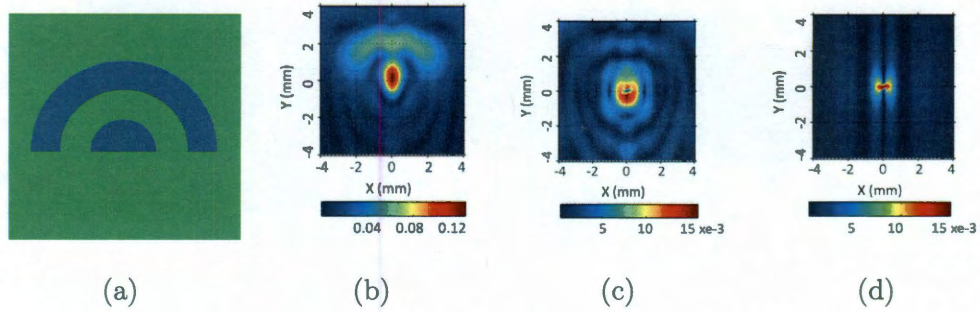


Figure 4.8 : (a) 180° FASA ring electrode with 13mm focal length; (b) vertical-component of particle displacement ( $u_z$ ); (c) radial-component of particle displacement ( $u_r$ ); (d) circumferential-component of particle displacement ( $u_\psi$ ).

this could be seen in figure-4.8 (b). The  $u_r$  due to 180° has its maxima located in the two quadrants where the transducer is not having any active source of ultrasonic waves (figure-4.8 (c)). Such a localized acoustic field is useful in focused acoustic applications. The rotational component due to 180° transducers has peaks in the (0°, 180°) directions. Typically, the maxima lobes of rotational component are close to the directions of the start-angle and end-angle of the transducer. This could be verified from this case also, as could be seen in figure-4.8 (d).

#### 4.4.3 90° Segmented FASA Element: the Basic Unit of DNA Shearing System

As described above, an acoustic lens built using 360° Fresnel rings focuses the acoustic waves at a focal point and the acoustic field pattern has radial and azimuthal symmetry in the x-y plane. The acoustic field varies in the z-direction and its intensity decreases as we move away from the lens. However, when the complete annular electrodes are broken into annular electrodes of incomplete rings (e.g. 90° or quarter rings), the acoustic field becomes unsymmetrical in the xy-plane, and produces spe-

cial lateral (or in-plane) force in the space. These lateral pressure variations cause the liquid placed over transducer to spin/mix and the vertical component causes the liquid to move in chaotic motion. Such an in-plane lateral acoustic field was first published in [29]. It is important to note that the vertical component of acoustic field is still accentuated due to constructive interference between the waves generated from different rings. In [29], a 90-degree segment of annular source, called Fresnel Annular Sector Actuator (FASA), was shown to generate strong lateral forces in the liquid placed over the transducer.

We designed a 90° FASA element with focal plane at a height of 13mm. The first-resonant thickness mode frequency of transducer is taken as 3.85MHz. The sound velocity inside water is assumed to be 1480 m/s. The maximum tile size is taken as 4mm by 4mm. We computed the radii of Fresnel rings which can fit in this size; two rings could fit in 8mm by 8mm area with the above design parameters. The radial ( $u_r$ ), circumferential ( $u_\psi$ ), and vertical ( $u_z$ ) components of particle velocity are computed using equations 4.15, 4.16, and 4.17 respectively, with integral limits for  $\psi'$  from 0 to  $\pi/2$  instead of 0 to  $3\pi/2$ . The plots for  $u_r$ ,  $u_\phi$  and  $u_z$  are shown in figure-4.9.

The simulated vertical particle displacement due to 90° transducer is shown in figure-4.9 (b); we notice that  $u_z$  has two peaks, first peak near the origin and second peak at the edge of first ring. Also, we observe that the first peak has circular symmetry while the second maxima resembles the shape of the 90° ring. Having distributed maxima of acoustic field or particle displacement helps in homogenous mixing of the fluid sample placed over the transducer. The radial component of particle displacements due to 90° sectored annular transducer is shown in figure-4.9 (c). As expected, the peak of  $u_r$  for 90° transducer, placed in the first quadrant, lies in

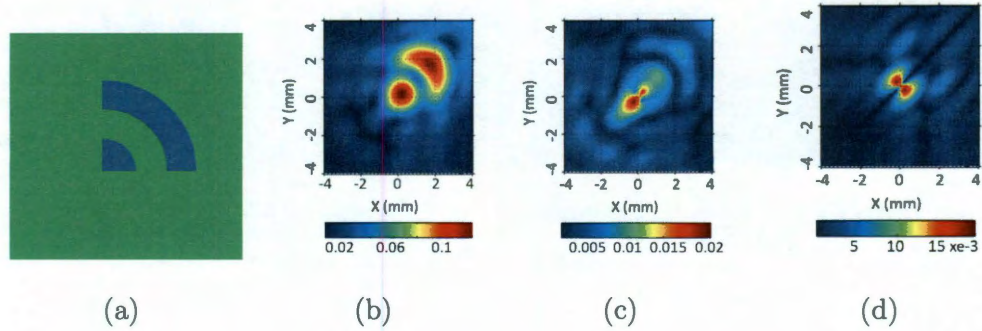


Figure 4.9 : (a) 90° FASA ring electrode with 13mm focal length; (b) vertical-component of particle displacement ( $u_z$ ); (c) radial-component of particle displacement ( $u_r$ ); (d) circumferential-component of particle displacement ( $u_\psi$ ).

the third quadrant because there is no active transducer element in the third quadrant to equalize the acoustic field generated towards third quadrant. The maximum rotational component of a sectorized transducer is in the plane perpendicular to the orientation of the rings of the transducer. For example, the 90° transducer placed in first quadrant has an orientation of 45°, its  $u_\psi$  has maximum intensity in 135° and 315° direction, as shown in figure-4.9 (d).

Finally, to compare transducers with different sector-angles, we plot the maximum acoustic particle displacements ( $u_z$ ,  $u_r$ , and  $u_\psi$ ) for these transducer patterns in figure-4.10. Figure-4.10 (a)-(c) plot the value of  $u_z$ ,  $u_r$ , and  $u_\psi$  normalized to electrode area. It is observed that the 90° transducer has higher normalized field than 180°, 270°, and 360° transducers. We also observe that the transducer with low sector-angle has higher normalized acoustic field. Figure-4.10 (d)-(f) show the plots of absolute value of  $u_z$ ,  $u_r$ ,  $u_\psi$  for 90°, 180°, 270° sectorized and 360° transducers. As expected, the absolute values of  $u_z$  and  $u_r$  increase with increase in sector angle because of increase in the active area of transducer which generates the ultrasonic waves. However, the rotational component ( $u_\psi$ ) increases with increase in sector angle and it is maximum

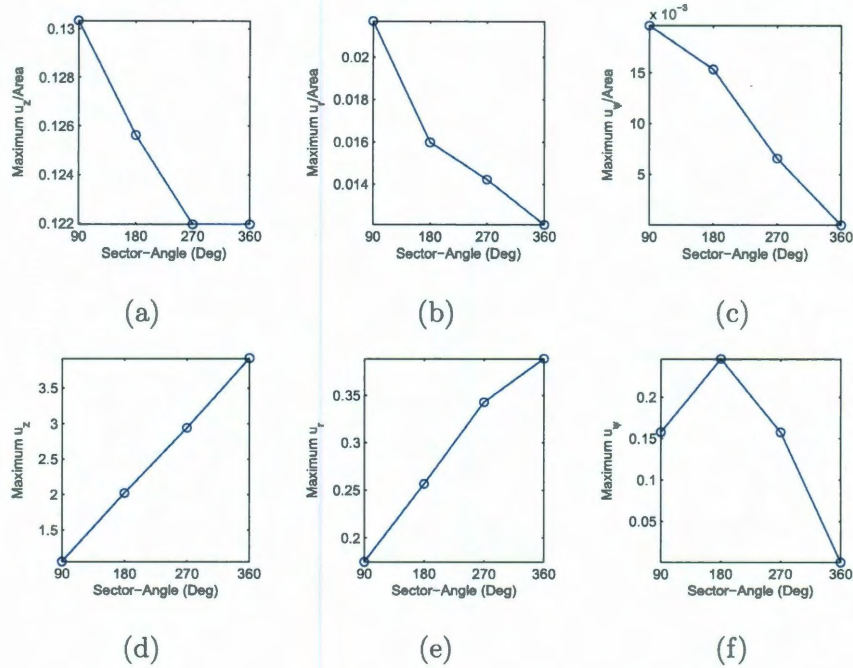


Figure 4.10 : Particle displacement for different sector angles (a)-(c)  $u_z$ ,  $u_r$ ,  $u_\psi$  per unit electrode area; (d)-(f) Absolute  $u_z$ ,  $u_r$ ,  $u_\psi$  .

for 180° transducer. It again decreases as we increase the sector angle from 180° and reaches to zero value for 360° ring transducer due to complete symmetry. We select 90° sector angle because we can build a 180°, 270°, 360° transducer by arranging more than one 90° transducers in an array. Also, we wanted to keep the number of transducers in an array to a low number to keep the requirement of number of separate RF signal low for the phased-excitation.

#### 4.4.4 Phased-Array Fresnel Annular Sector Actuators (FASAs)

When two or more FASA elements are placed adjacent to each other, we call such an arrangement as array of FASA elements. Each FASA element generates its own acoustic field in the space over it. Typically, all the FASA elements used to make



an array are of same type. In other words, electrode pattern of all FASA elements is same and an array is formed by placing different FASA elements near one another on a piezoelectric slab. By arranging the FASA elements in different types of array, one can generate different type of acoustic field-patterns targeting different applications. For example, if we make an array by putting multiple  $90^\circ$ - FASA elements in a straight line, we can transport the liquid in a horizontal line. It is shown in [47] that the liquid can be transported from one place to another at a controlled speed; a speed upto 123 m/s is reported in that work. We can also use dissimilar FASA elements to make an array of FASA elements. For example, we may use one  $90^\circ$ -FASA element, two  $60^\circ$ -FASA elements and one  $150^\circ$ -FASA element to make a circular array of dissimilar FASA elements. Such an array will have a unique acoustic field pattern in the space which could be used in special applications.

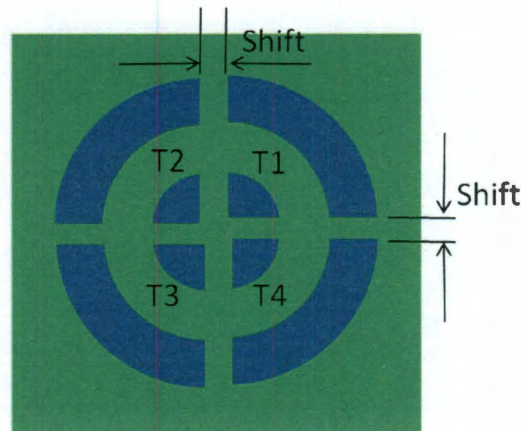


Figure 4.11 : Proposed piezoelectric transducer structure based on array of four  $90^\circ$  Fresnel annular actuators.

In the proposed microfluid-processor or DNA shearing system, we use four  $90^\circ$ -FASA elements and arrange them in a circle to cover the entire bottom of the fluid container. Such a transducer pattern is shown in figure-4.11, wherein, T1, T2, T3 and

T4 represent the four 90° transducers and the “shift” denotes the distance between any two adjacent transducers in the array. The value of “shift” is either chosen to be some multiple of wavelength or it is decided based on the maximum tile size allocated to the transducer area. Depending on the value of shift between two transducers the transducer has localized or distributed maximum acoustic field in space.

Each FASA element in the array has a dedicated RF-circuit which provides us the freedom to excite each FASA element at different voltage, frequency, phase, duty cycle, and so on. We leverage this freedom and excite the FASA elements with four RF signals of same voltage, frequency, repetition-rate and duty-cycle but at different phase angles. By changing the phase difference between RF-signals applied to different FASA elements we are able to generate different acoustic field-patterns in the liquid. Different acoustic fields produce different particle velocities (i.e. different types of vortexes) in the liquid sample. As we notice from the simulation results in figure-4.12 (a)-(1), the particle displacement fields ( $u_z$ ,  $u_r$ , and  $u_\psi$ ) get delocalized in space as we increase the value of “shift” from 0 to  $5\lambda$ .

Four transducers are excited by four separate RF amplifiers in our fluid processing system. The RF signals for T1-T4 are given by equations (4.18):

$$RF_i = D_i(t)V_i \sin(\omega t + p_i) \quad (4.18)$$

Where,  $i=\{1, 2, 3, 4\}$  denotes transducers T1, T2, T3 and T4 respectively,  $V_i$ ,  $D_i(t)$  and  $p_i$  are the peak voltage, duty cycle and phase of RF signal applied to  $i^{th}$  transducer. Having independent RF excitation for each transducer helps in switching-on and-off or applying a phased excitation that greatly improves the fluid processing or DNA shearing process based on sonication.

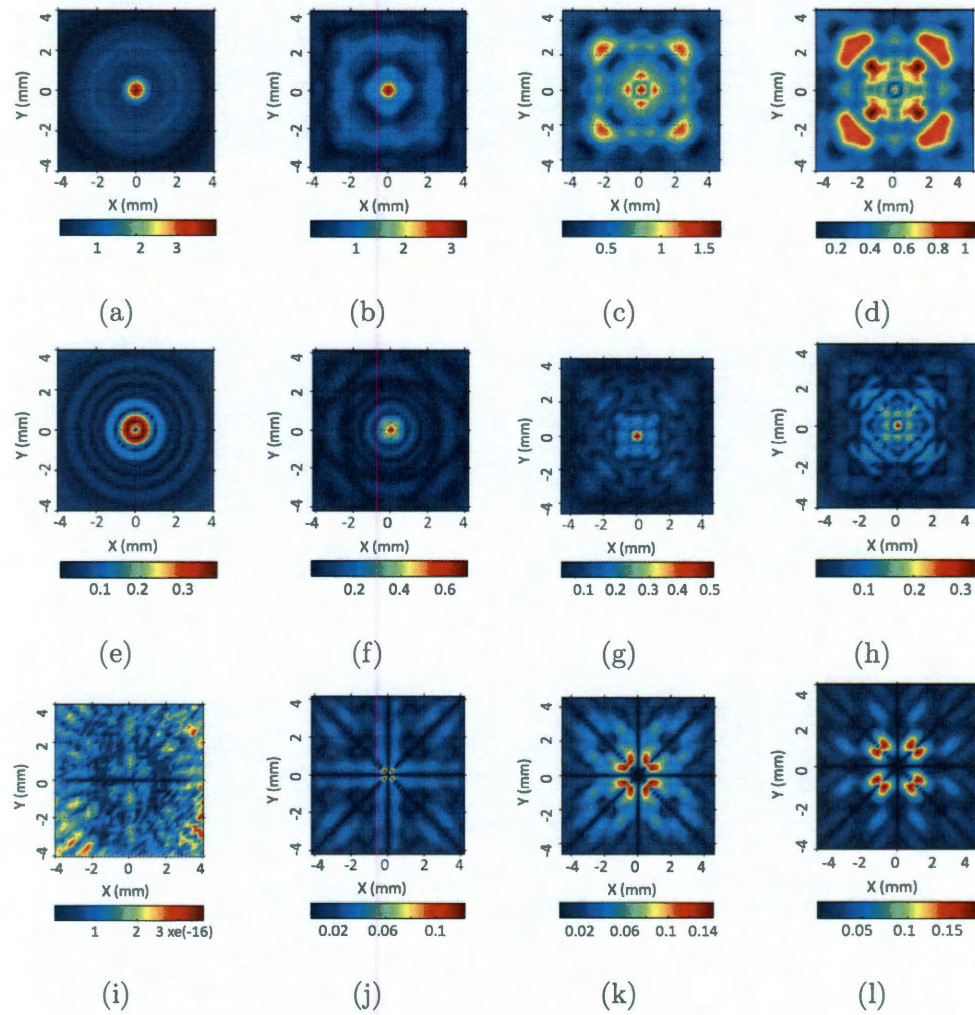


Figure 4.12 : Particle displacement due to an array of four 90° sectored annular transducers: (a)-(d)  $u_z$ :  $shift=0$ ,  $\lambda$ ,  $3\lambda$ ,  $5\lambda$ ; (e)-(h)  $u_r$ :  $shift=0$ ,  $\lambda$ ,  $3\lambda$ ,  $5\lambda$ ; (i)-(l)  $u_\psi$ :  $shift=0$ ,  $\lambda$ ,  $3\lambda$ ,  $5\lambda$ .

## Chapter 5

# Fabrication and Characterization of Piezoelectric FASA Element

### 5.1 Photo-lithography Based Fabrication Process

Most of the ultrasonic transducers are made of piezoelectric materials. Lead zirconate titanate (PZT) is the most common piezoelectric material which is used to build the transducers. PZT material is initially available in the powder form; a very high temperature and pressure is applied to make an amorphous solid out of PZT powder. The large solid block is cut into shape of plate by very high speed (high rpm) crystal cutters. We procured PZT wafers from different vendors. all of whom have more or less same fabrication process. The electrodes of particular shape are patterned on both surfaces (top and bottom surfaces) of PZT wafer using standard semiconductor photo-lithography process. Typically, PZT wafers are available with nickel evaporated on its surfaces; 75% nitric acid ( $HNO_3$ ) is used to remove the nickel from top and bottom surfaces of PZT [30].

A positive SU-8 photoresist is coated on both surfaces of PZT. The SU-8 layers have front-to-back aligned patterns for the complete overlapping of top and bottom electrodes of PZT. The SU-8 mask layers is exposed to UV light for a specific time and hence, only the light exposed region of photoresist becomes soluble to photoresist-developer. The extra metal, corresponding to light-exposed region of mask, is removed leaving behind only the overlapping electrodes of desired pattern on both sides of PZT.

All external contacts to the FASA transducer are then to be made from the bottom side of the transducer. Each FASA effector has a dedicated RF-driving circuit.

## 5.2 Characterization

Each FASA element is characterized for its resistance and reactance values at different frequencies. Impedance values of FASA elements at different frequencies are obtained from smith-charts plotted using Agilent Network Analyzer (E5061B) [49]. Based on the impedance-plots for every FASA element we find precise series and parallel resonance frequencies for the element. Both, at series and parallel resonance frequencies, the impedance of piezoelectric FASA element is purely resistive. However, the impedance is minimum at series resonance and hence, the charging and discharging current flowing through FASA element is maximum at series-resonance frequency for a fixed input-voltage. Therefore, we operate at series resonance frequency. Also, we know from Mason's model that the particle velocity, due to stress waves generated from piezoelectric plate in response to RF signal, is directly related to the electrical current flowing through the piezoelectric plate. High particle velocity generates powerful vortexes and shear forces, so, we operate the FASA element at its series resonance frequency. Further, we plot RF scattering-plots, in particular  $S_{11}$  plots, for FASA elements using network analyzer; based on those plots we find the frequency at which the power-reflection at input port of FASA element is minimum.  $S_{11}$  is the ratio of the reflected to the incident signal; it provides a measure of the complex electrical input impedance of the transducer. We use this information to design/procure a suitable power amplifier for feeding the power to FASA element. Typical  $S_{11}$  and smith-chart plots for FASA element with water loading are shown in figure-5.1.



Figure 5.1 :  $S_{11}$  plots for a sample piezoelectric FASA element plotted using Agilent E5061B network-analyzer. (a) log magnitude plot; (b) Smith impedance plot.

The  $S_{11}$  plot on smith chart, with impedance scale, for a sample FASA element is shown in figure-5.1(b). The two markers shown in the smith-chart denote the frequencies at which the impedance of FASA element, as seen from input port, is pure resistive. The first marker (placed at 4.0677MHz) corresponds to series resonance of the transducer at which the impedance of the transducer is minimum. While the second marker (placed at 4.168MHz) represents the parallel-resonance frequency of transducer. As explained above, this transducer should be operated at 4.07 MHz for optimum performance.

We want to operate at the frequency at which there occurs minimum reflection at the input port. The operation at that frequency will make sure that a large fraction of RF power generated by class-E amplifier is absorbed by the transducer element. It is important to note that this frequency may not be same as the series or parallel resonance frequencies of the transducer element, as discussed above because this includes loading from coupling fluid and the sample placed over the transducer.

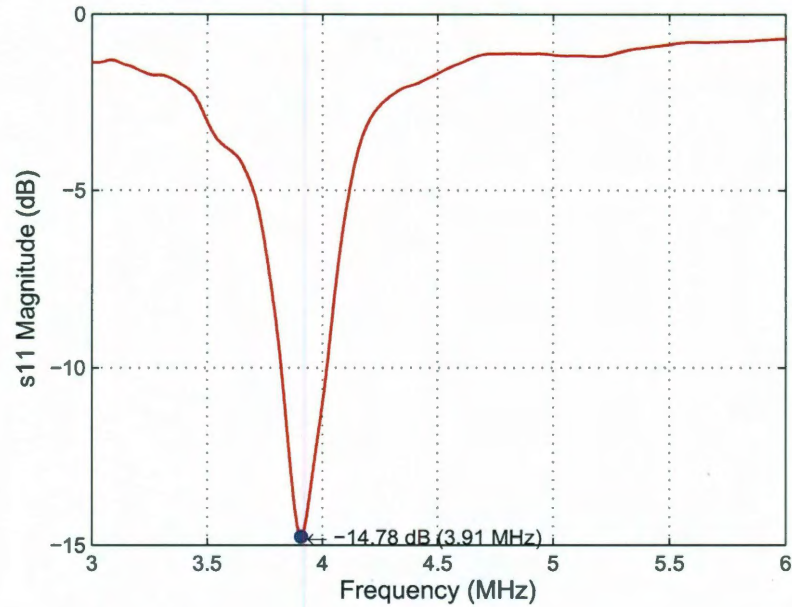


Figure 5.2 :  $S_{11}$  plot of a fresnel annular sector actuator patterned on a transducer obtained from Piezo Systems, Inc.

### 5.3 Equivalent Electrical-Circuit of Piezoelectric Transducer Based on its Impedance Characterization

Piezoelectric transducer is excited by RF signal of appropriate frequency to generate ultrasonic waves. We use class-E topology to generate RF-signals [50, 51, 52]; for RF amplifier, piezoelectric transducer elements acts as the electrical load. This load is not purely resistive; the transducer element offers different resistance, inductance and capacitance at different frequencies. Also, the load varies depending on the number of transducer elements we connect across the output of RF amplifier. All these varying parameters make the analysis difficult, because we have to consider variable load during the analysis of RF amplifier in the desired frequency range. It is important

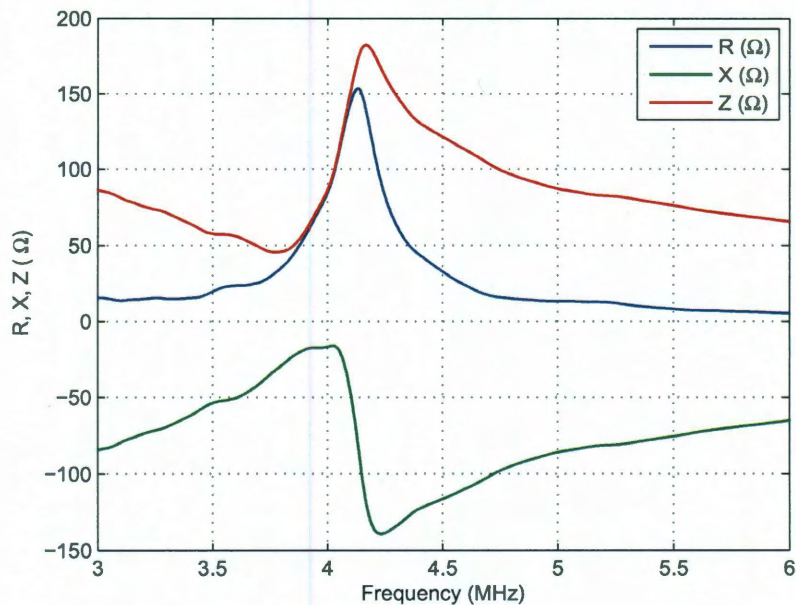


Figure 5.3 : Resistance (R), reactance (X) and impedance (Z) plots of a Fresnel annular sector actuator designed on a transducer obtained from Piezo Systems, Inc.

to note here that one can not drive all four FASA elements of a shearing module by single RF-amplifier, provided one uses phasing circuit between the RF amplifier and FASA elements. It is difficult to control/add phasing between high-voltage RF signals, so, the phasing is achieved using digital circuit. Hence, four RF-amplifiers are used to generate four-different RF signals to achieve any possible phasing between them.

The MEMS based transducer element designed on a piezoelectric plate has different impedance at different frequencies. Both real and imaginary parts of impedance are functions of frequency. At low frequencies the impedance of the piezoelement is capacitive and hence, it is typically modeled by a series RC circuit. As we increase the frequency of the excitation to the piezoelement, there occurs a resonance point



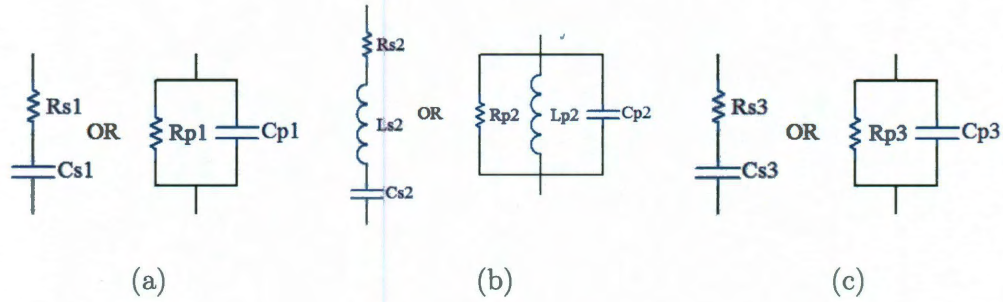


Figure 5.4 : Circuit models for FASA element at different operating frequencies. (a)  $f < f_s$ ; (b)  $f_s < f < f_p$ ; (c)  $f > f_p$ .

where the impedance of the piezoelectric element reaches to its minimum value. The impedance at this frequency is purely resistive. This frequency is typically represented by  $f_s$  and is called as series resonance frequency. As we increase the frequency further, impedance of the piezoelectric element starts becoming somewhat inductive and hence it is modeled by a resistance connected in series/parallel to a series/parallel connection of capacitor and inductor. By further increasing the frequency, there arrives a point where impedance of the transducer with piezoelectric plate becomes maximum and purely resistive. This frequency is called as parallel resonance frequency,  $f_p$ . The electrical models for piezoelectric transducers operating at different frequencies are shown in figure 5.4 (a)-(c) [53].

Ideally, we would like to operate at one of these two resonance frequencies to minimize the reactive power and maximize the actual power being delivered to transducer element. At both these resonance frequencies, piezoelectric transducer element behaves as a purely resistive load and that also allows us to leverage the circuit analysis presented by Sokal [52] for the class-E amplifier circuit. This way, we were able to find the values of different inductors ( $L_1$  and  $L_2$ ) and capacitors ( $C_1$  and  $C_2$ ) by simulating the circuit in SPICE.

## Chapter 6

### Complete Architecture of Proposed DNA Shearing System

The proposed DNA shearing system consists of mainly three physical domains. These domains are- Electrical Domain, Piezoelectric Domain, Acoustic-fluid Interaction Domain. The block diagram of proposed DNA shearing system is shown in figure-6.1.

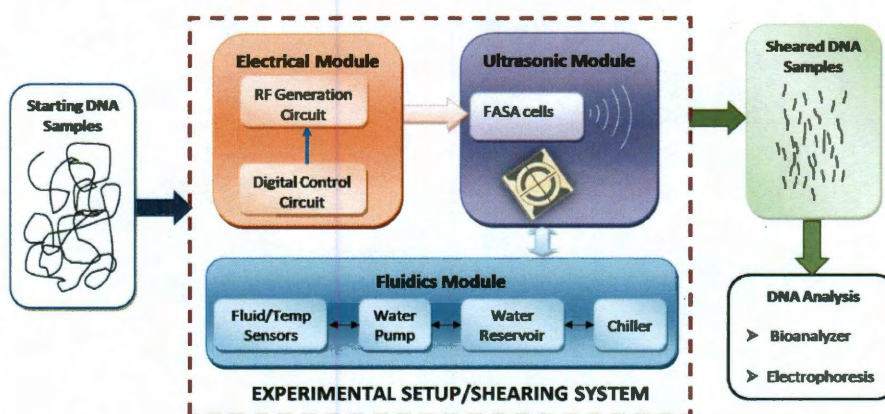


Figure 6.1 : Block diagram of the proposed DNA shearing system

#### 6.1 Electrical Domain

The electrical domain constitutes of different digital, analog and RF components used to build electrical circuitry of the system. The clocking circuit and control-signal generation circuitry are the main digital components and they are implemented in Cyclone III family of FPGA from Altera. Since one shearing module is made of four

90° FASA elements and each FASA element is excited by separate RF signal, we need four clock signals of appropriate frequency and phase to drive four elements. The clock signals are not just continuous square pulses of a particular frequency, instead, they are generated by the logical AND operation of two different frequency signals- fast clock and slower clock. It is pictorially shown in figure

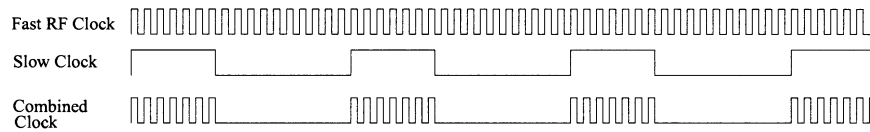


Figure 6.2 : Combined clock: logical AND of fast RF clock (MHz) and slow clock at repetition rate

The frequency of the faster clock signal is the same as the first thickness-mode resonant frequency of piezoelectric transducer. For the transducer used in our system, this frequency is around 4MHz. The frequency of slower clock signal is commonly referred as Repetition rate or simply replate and its value is determined empirically on the basis of desired DNA fragment size. The duty cycle of slower clock decides the number of fast (RF) pulses in a burst, with burst rate same as the frequency of slower clock. The frequency of fast clock decides the frequency of square pulses within a burst.

It is important to choose proper values for the frequency and duty cycle of the slower clock because these determine the time required to shear the DNA and the size distribution of the sheared DNA. If we decrease the frequency of replate, the number of continuous RF pulses in a burst will increase which could generate strong enough acoustic pressure to cause liquid ejection or splashing of liquid inside the tube. On the other hand decreasing the duty cycle and keeping the replate low will not be able to generate enough acoustic waves and therefore does not provide shearing. This is

Table 6.1 : Effect of Duty Cycle and Repetition Rate (slow clock) on the DNA Sample

	Low Repetition Rate ( $0 - 500Hz$ )	High Repetition Rate ( $> 500Hz$ )
Low Duty Cycle	Not enough Acoustic Pressure	Ejection Dominated Nebulization
High Duty Cycle	Ejection Without Nebulization	Ejection and Heating

also summarized in the table 6.1.

We generate four such combined clock signals, also called RF clocks, for four FASA elements. The RF clocks are generated using Aletra FPGA which has TTL compatible outputs with 3.3V as high and 0V as logic low. Each RF clock is used as an input to an RF amplifier which generates a high-voltage RF signals with frequency and phase profiles same as the applied RF clock. This means that we require four separate RF circuits corresponding to four RF clock-signals. We chose to implement class-E RF amplifiers to generate high-voltage RF signals due to their high power-efficiency [52].

**Class E Amplifier:** The circuit diagram of class-E amplifier is shown in figure-6.3. Class-E amplifier circuit has an active device or switch, e.g. power MOSFET, to control the operation of series tank circuit containing  $L_2$  and  $C_2$  lumped elements [52]. The inductor  $L_1$  has a large value to prevent any harmonics being added to the supply voltage  $V_{CC}$  or  $V_{DD}$ . The value of supply voltage is allowed to vary between 5V to 140V in the proposed DNA shearing system. When input to the active device is high, the switch is closed and charge stored on capacitor  $C_1$  will discharge immediately into ground through the switch. To avoid power dissipation in the switch, it should be

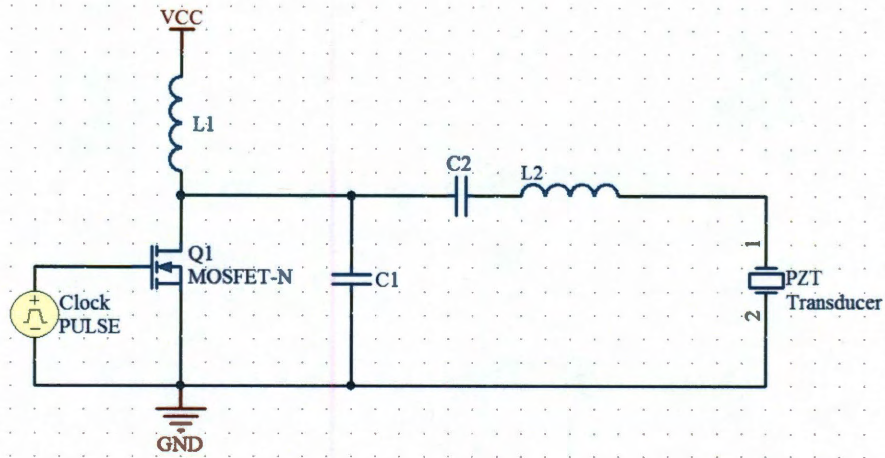


Figure 6.3 : Circuit diagram of class-E amplifier used to generate RF-signal for exciting the transducer [52].

made sure that the voltage at drain/collector of transistor is reduced to zero before switching ON the active device. Reducing the voltage at drain/collector to zero before the active device becomes ON means that we are discharging the charge stored on  $C_1$  towards the load side and not through the switch. This is required for increasing the overall efficiency of RF amplifier.

On the other hand, when input to the active device (transistor) is low, the switch is open and the capacitor  $C_1$  is charged to supply voltage  $V_{CC}$  through RF-choke  $L_1$ . Values of different inductors and capacitors are decided in such a way that the circuit delivers maximum power to the load,  $R$ . The analysis presented in original Sokal's paper assumes that the load is pure resistance. Based on this assumption it was possible to find the optimum values of different circuit elements.

## 6.2 Piezoelectric Domain

When the RF signal generated from class-E amplifier is applied across the two electrodes of piezoelectric plate, stress waves are generated inside the transducer. This is called as reverse-piezoelectric effect and is explained in detail in section 3.2. For a thickness excited transducer, these stress waves propagate in both upward and downward side. Depending on the acoustic impedance of the medium above transducer, a part of acoustic waves will be transmitted through the material-boundary in the path and others will be reflected back towards the transducer. More often than not, the waves after multiple reflections at different material-transitions become too weak to do any useful work and hence dump their energy in to the coupling fluid. The circulating coupling fluid extracts this energy and keeps the temperature of the bath or the DNA sample in the tube within the allowable limits.

## 6.3 Acoustic-fluid Interaction Domain

Acoustic field generated from the piezoelectric transducer (FASA) creates vortexes and shearing forces in the sample. The frequency of acoustic field is the same as RF frequency (in MHz). The liquid particle tries to move at the RF frequency; however, the viscous force dampens (like a resistance) the acoustic energy, converting some of the energy into heat. Due to this reason, a part of acoustic energy gets converted in to heat inside the sample and can increase temperature of the sample if precautionary steps are not taken. We use coupling fluid in our system to maintain the temperature of DNA sample within allowable limit during shearing process. It is important to keep the temperature of sample within limit (typically 90°C), after which the DNA gets denatured. It is also reported that if we let the temperature of DNA to go above

45 degree C, the DNA sample becomes AT-rich and the proportion of GC decreases. To avoid these adverse effects, we circulate the water to extract the heat dumped in to sample and an external chiller is used to keep the temperature of circulating water, and hence of DNA sample, at user specified value. In addition to its use as cooling fluid, water has another important purpose in our system, that is, it acts as coupling fluid. In order to efficiently transfer the stress waves generated inside PZT material to external medium, the relative acoustic impedance of the material which comes in direct contact with the transducer is critical. The typical acoustic impedance of commonly used PZT materials is between 30 and 40 MPa.s/m. The acoustic impedance of water is 1.5 MPa.s/m and that of air is 420 Pa.s/m. Since the difference between acoustic impedances of water and PZT is smaller than the difference between acoustic impedance of air and PZT, the transfer of acoustic waves happen more efficiently at PZT-water interface than at PZT-air boundary. Hence, water helps in efficient propagation of acoustic waves from transducer to the sample. The sample is placed in a plastic tube, which also reflects a part of acoustic waves from its bottom. To minimize these kind of losses, we should use a quarter wave matching layer at every material interface, viz. transducer-water interface and water-tube interface.

Figure-6.4 shows the DNA shearing process in action. This figure shows 96 transducer (FASA) modules designed on a large piezoelectric transducer. The center to center distance between adjacent transducers is such that each module aligns exactly with the 96-well standard microplate. For the experiment purpose,  $100\mu L$  sample of Lambda-DNA was put in a matrix-tube from Thermo Scientific. The concentration of DNA was  $20\text{ng}/\mu L$ . The tube was held at a height of 7mm from the transducer surface; the optimal height where the DNA shearing is maximum is found empiri-

cally. The figure also shows the atomized DNA inside the tube; we termed it as cold smoke. The DNA sample leaves the meniscus in the form of smoke when sonication is applied to the sample and the smoke does not escape out from the tube, even if the tube is not covered from the top. Hence, this smoke is not same as conventional smoke which would have escaped from the tube. The smoke rises to a certain height in the tube and comes down back to the sample and converts in to liquid again. The smoke generation is a continuous process. In this whole process some of the smoke comes in contact with the side walls of tube and converts in to liquid droplet. The size of droplets stuck on walls increase over time due to continuous smoke coming in contact with walls. But some of the small droplets remain stuck on the walls which causes the loss of DNA sample, an undesirable thing in the DNA shearing process.

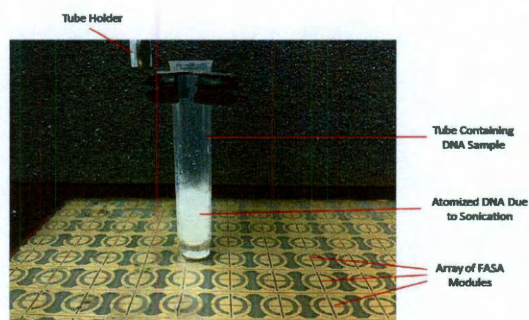


Figure 6.4 : DNA shearing in action



## Chapter 7

### Experimental Results

We performed many shearing experiments on real DNA samples. Mainly, we performed shearing experiments on three types of DNA samples- Lambda DNA, mouse genomic DNA and human DNA. Since human DNA and mouse genomic DNA are relatively more expensive than the Lambda DNA from E. Coli, we used Lambda DNA for our most of the experiments. As discussed later in this chapter, we observed that the shearing results are independent of the source of the DNA. So, all the results obtained on Lambda DNA are reproducible on DNA from other sources also.

#### 7.1 DNA Fragment Analysis Tools

Gel-electrophoresis and Agilent Bioanalyzer 2100 are two standard methods of analyzing the DNA shearing results [54, 55, 56].

1. *Gel-Electrophoresis*: In a standard gel electrophoresis system, DNA, along with reference markers (having known fragment sizes) is loaded in the wells of the gel solution and an electric field is applied between the two electrodes, placed at two ends of the gel [54, 55]. Due to the ionic properties of DNA, the DNA sample starts moving toward the negative electrode. The speed at which the DNA fragments travel in the gel is decided by the DC voltage applied between the electrodes. Further, the smaller DNA fragments move at higher speed than larger DNA fragments. This means that at any particular instance of time, after

the electric field is applied, the DNA fragments get separated in the gel based on their base-pair length. Both markers and DNA sample under test propagate in the gel under the influence of applied electric field. Since, the sizes of DNA fragments in marker wells are known, one could find the range of DNA fragments in the DNA sample also. After a reasonable time, typically 30 mins for standard gel-electrophoresis and 10 mins for Lonza gel-electrophoresis system, the DNA fragments are well separated in the gel. As the electric field is applied only in one-direction, the DNA fragments travel only in one direction. Before loading the DNA in to wells of gel, a fluorescent dye is mixed with the DNA sample which fluoresces in the presence of ultraviolet light. The fluorescent image is then captured using UV camera and the image shows the different fragments present in the sample. One such image is shown in figure-7.1 (b); it is captured using a gel-system, as shown in figure-7.1 (a), from Lonza company [55]. The intensity of gel image is directly proportional to the number of fragments of particular size.

Before sequencing the DNA fragments using DNA sequencers, the DNA fragments lying in the desired fragment-size range are selected by cutting the gel and then chemically processed for any repair of the ends of fragments. The advantages of gel-electrophoresis are that it is relatively cheaper than other methods and it provides fairly good analysis of DNA fragment sizes in a DNA sample. However, standard gel-electrophoresis provides only qualitative analysis of DNA fragments in a sample. For example, if a DNA sample has all fragment sizes ranging from 100 bp to 3000 bp, the gel-electrophoresis image will have a large smear ranging from 100bp to 3000bp. The intensity of gel-image is used to predict the mean size of DNA fragments. Other tools and methods should be

used for more quantitative analysis of DNA fragments in the DNA sample.

2. *Agilent Bioanalyzer 2100*: Agilent Bioanalyzer is another tool to analyze the molecular weights (or base-pair length in more common language) of DNA fragments in the DNA sample [56]. It provides more quantitative analysis of the fragment sizes present in the sample. The basic principle of finding the DNA fragment size is same in both standard gel-electrophoresis system and Bioanalyzer - both methods rely on the difference in travel-speed of different fragment sizes inside gel under the influence of electric field. However, Bioanalyzer provides a more quantitative analysis of fragment sizes in the DNA sample. For analyzing the sample using Bioanalyzer, DNA samples along with reference marker (called ladder more often) are loaded into the small wells of microfluid chips using a well-defined procedure and a software controlled method is used to generate the distribution graphs for base-pair lengths present in the DNA sample. There are two types of chips available from Agilent- normal-kit and high-sense kit. Normal chips require DNA to be of higher concentration, while the high sense kit, as the name implies, could analyze the DNA with low concentrations also (as low as 500pg/uL). One has to follow same procedure for both normal and high-sense kits/chips to plot the fragment sizes in a sample; the difference being that the high-sense kit provides more accurate analysis with lower DNA concentrations.

## 7.2 DNA Shearing Protocol and DNA Shearing Results

To achieve different shearing results, one just needs to find proper experimental settings, also called shearing protocol. A typical shearing protocol comprises following

parameters: peak RF voltage, RF frequency (decided by the thickness and material of piezoelectric transducer), repetition rate (duty cycle) of RF signal, phasing between RF signals applied to different transducers in the transducer-array, sonication time, volume of DNA, concentration of DNA, type of DNA, starting size of DNA, target mean size and distribution. The results presented in this thesis are preliminary results for the shearing experiments performed on the proposed system. We are still optimizing the shearing protocols for obtaining user defined DNA fragments in minimum time.

The shearing protocol is decided based on following parameters: the starting size of DNA, target mean fragment size, fragment distribution, volume of DNA, concentration of DNA. Based on the experiments done on our system, we observed that the peak to peak RF voltage used to excite the transducer, duty cycle of the RF signal, and the sonication time has great effect on the final mean DNA fragment size.

Figure-7.1 shows the results of four sample experiments performed on Lambda DNA. In the first experiment, we used peak-to-peak RF voltage applied to the transducer array as 140V. The repetition rate of the RF signal is kept at 420Hz for all the experiments. After 15 minutes of sonication at 140V at 1% duty cycle, the mean size of DNA fragments is found to be about 1854bp. In the second experiment, we wanted to decrease the mean fragment size of sheared DNA. To this end, we increased the voltage to 165V and decreased the duty cycle to 0.75% to keep the same intensity of sample processing and sheared the lambda DNA to mean fragments of 1350bp size (third channel of the gel image in figure-7.1). We further increased the voltage to 190V and 215V and decreased the duty cycle to 0.5% and 0.25% respectively; the mean DNA fragment size obtained at these voltage settings are 700bp and 370bp respectively. The sheared DNA were analyzed using both standard gel-electrophoresis

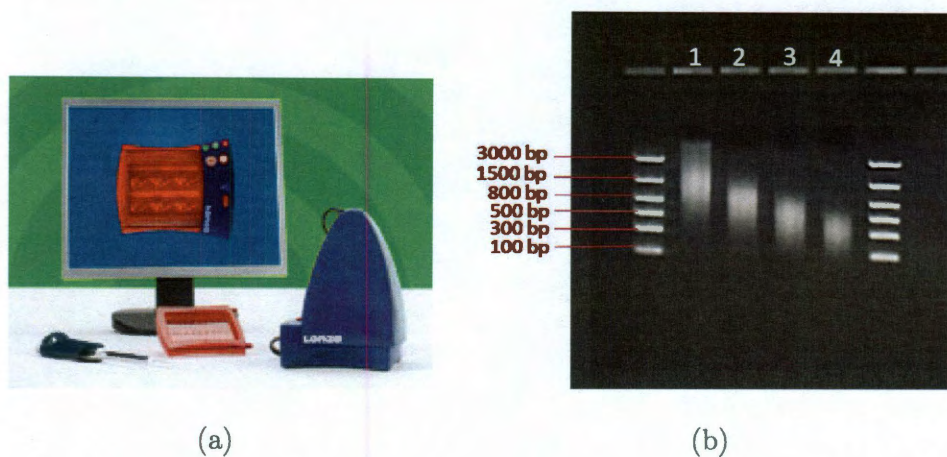


Figure 7.1 : (a) Gel-electrophoresis system [55] (b) gel-image of Lambda DNA(48kb)[Concentration  $5\text{ng}/\mu\text{L}$ ] sheared to different peak fragment sizes using the proposed shearing system

and Agilent Bioanalyzer 2100. The gel-image for these four experiments is shown in figure-7.1. Hence, Lambda DNA with starting size of 48 kb was successfully sheared to different fragment sizes using the proposed DNA shearing system. We were able to achieve fragment sizes ranging from 300bp to 1.5kbp using different experimental conditions. The sheared DNA was loaded in to a gel electrophoresis system (electrophoresis is used to find the size of DNA fragments); the gel-image as captured by the imaging system (figure-7.1-(a)) is shown in figure-7.1-(b).

We studied the effect of different parameters on the shearing. Some of these parameters include the starting size of DNA, type of DNA to be sheared, concentration of DNA, volume of DNA, DC voltage, frequency of operation, repetition rate (burst rate), number of pulses in a burst and sonication time. We present the effect of each of these in this thesis.

#### 1. Effect of Sonication Power on DNA Shearing Results: Eventhough dif-

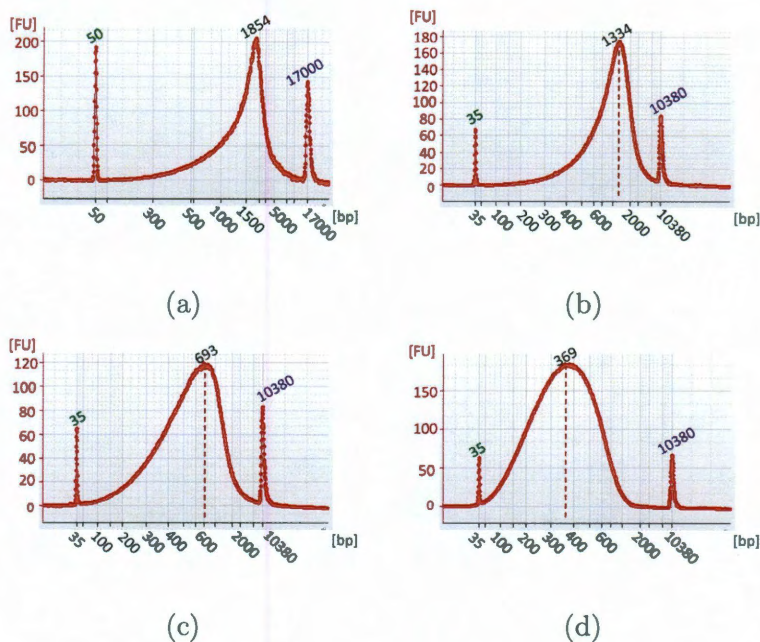


Figure 7.2 : Agilent Bioanalyzer plots for the four shearing experiments (a) mean fragment size: 1850; (b) mean fragment size: 1350; (c) mean fragment size: 700; (d) mean fragment size: 370.

ferent sonication based DNA shearing systems utilize different types of ultrasonic waves for DNA shearing, one thing is common in all methods - ultrasound energy. Most of the sonication based methods generate higher than required sonication energy and then empirically find the energy levels required for obtaining different mean fragment size of sheared DNA. For example, in focused acoustic DNA shearing technique, one has to attenuate the ultrasonic energy to obtain large DNA fragments; large unattenuated ultrasonic energy is used to generate small fragments. Hence, the DNA fragment size is controlled by the different attenuation levels, typically obtained by using sample tubes made of different materials or different thicknesses. However, in our proposed system,

we generate a controlled ultrasonic energy and we do not rely on the attenuation of sonic energy for obtaining different sizes of DNA fragments. We use uniquely designed piezoelectric transducer to generate special ultrasonic waves (having both converging and vortexing effects inside DNA sample) in our DNA shearing system. The intensity or power of ultrasonic waves generated from the transducer is directly related to the peak RF voltage applied across the transducer. We varied the peak-to-peak RF voltage to see its effect on DNA shearing results, we observed that the mean fragment size reduces with increase in voltage. The result of such an experiment are presented in figure 7.1 (b) and 7.2.

We found that the mean size of fragmented DNA is largely decided by the peak-to-peak voltage RF signal applied across the piezoelectric transducer. At supply voltage of 73 volts DC to class-E RF amplifier, the mean size of sheared DNA is about 800 base-pairs (bp). As we increase the voltage, the mean fragment size reduces.

- 2. Effect of Sonication Time on DNA Shearing Results:** For sonication based DNA shearing methods, sonication time is a very important parameter of the shearing protocol. The total sonication energy dumped into a DNA sample is the product of sonication power and the time. So, with increase in time, it is expected that the DNA will be fragmented more. We performed a controlled experiment at 215V peak-to-peak RF voltage with 50uL and 100uL of DNA sample. The results of these two experiments are shown in figure 7.3 and 7.4. The initial Lambda DNA had 48kbp size. A plot showing the comparison of DNA shearing results for these two experiments is shown in figure 7.5.

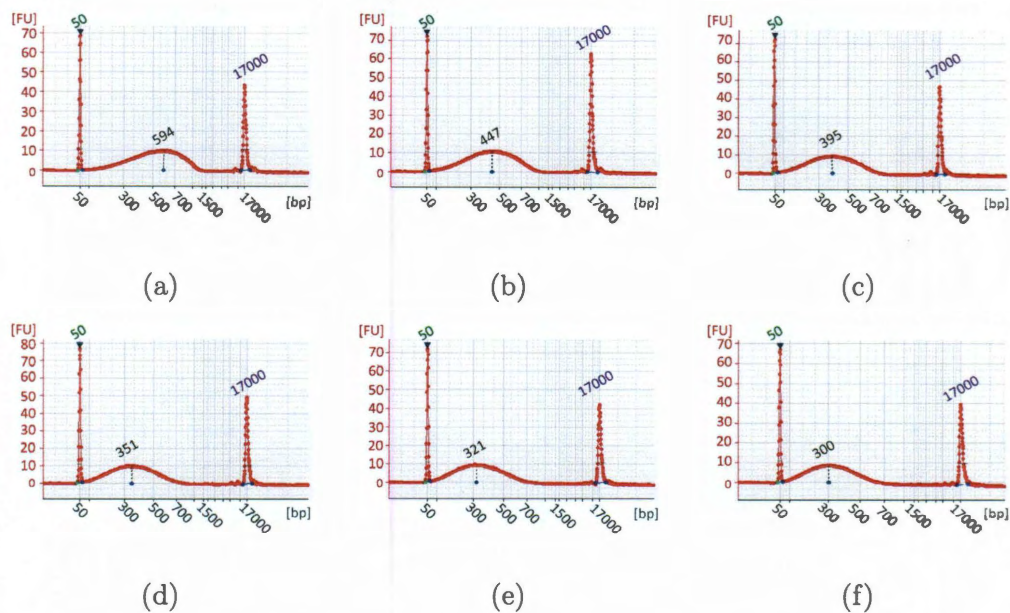


Figure 7.3 : Agilent Bioanalyzer plots for a 50uL DNA sample sonicated for different time durations (a) 10 mins; (b) 20 mins; (c) 30 mins; (d) 40 mins; (e) 50 mins; (f) 60 mins.

**3. Effect of Volume of DNA Sample on Shearing Results:** Since ultrasonic based DNA shearing technique rely on the ultrasound wave, the medium through which the wave propagate affects the amount of energy actually being dumped in to the sample. Further, if we assume that a particular amount of energy is required to break the bonds between nucleotides, higher volume of DNA sample would require more ultrasonic energy. So, for most of the ultrasound based DNA shearing systems, more ultrasonic energy is required to process higher volume of DNA. However, in our technology, the shearing is achieved by converging and vortexing properties of the ultrasonic waves and hence, the volume of DNA sample has different impact on the shearing results. We use converging effect of the acoustic wave to break the meniscus of the sample inside the



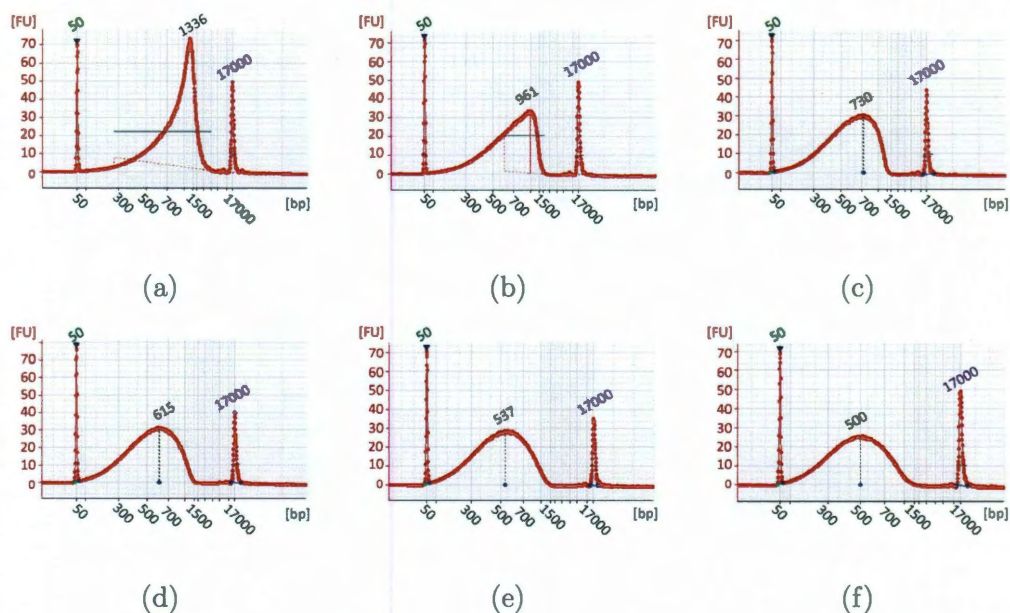


Figure 7.4 : Agilent Bioanalyzer plots for a 100uL DNA sample sonicated for different time durations (a) 10 mins; (b) 20 mins; (c) 30 mins; (d) 40 mins; (e) 50 mins; (f) 60 mins.

sample and vortexing effect to mix and recirculate the DNA sample for getting homogeneous shearing. For lower volume of DNA sample, the surface tension is higher than for a larger volume of sample, so we need little high duty cycle of RF signal to break the meniscus. We have experimented with sample volumes ranging from 25uL to 120uL. Based on experimental results, we observed that, for the same sonication time, the mean fragment size for 50uL DNA sample is lesser than the mean fragment size achieved in 100uL. This could be observed from the experimental results shown in figure 7.5.

With the current experimental setup, we observed that one could use any volume between 50uL to 120uL. With more robust system implementation and better optimized shearing protocol, the range of volumes that could be sheared using

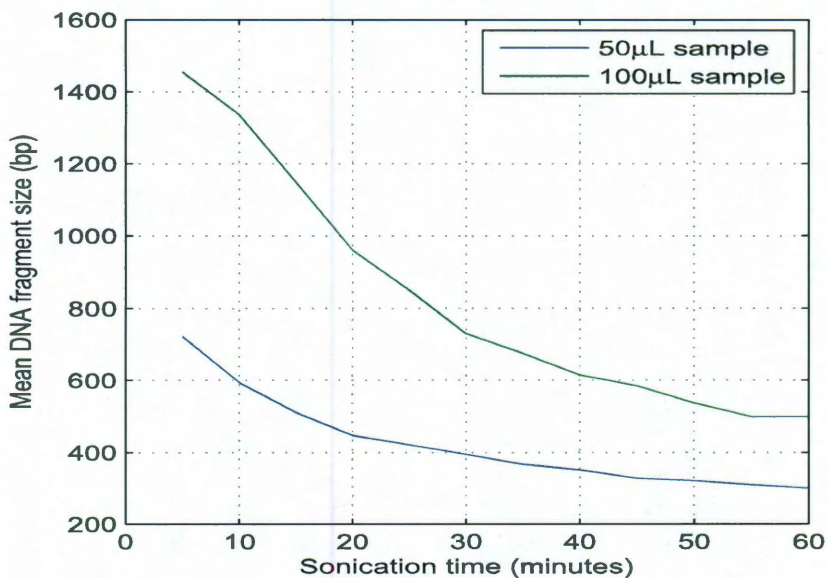


Figure 7.5 : Shearing results on Lambda and Genomic DNA for 15 mins, 30 mins, and 1 hour sonication time.

the proposed phased-array transducer would be higher. In fact, the transducer is fabricated using MEMS based process, so one could use the proposed transducer structure in a lab-on-a-chip device. In a lab-on-a-chip device, very small volume of DNA sample (pL to nL) could be transported through the microchannels and the DNA could also be sheared using the integrated transducer array based on FASA element.

4. **Effect of Concentration and starting size of DNA Sample on Shearing Results:** DNA is typically diluted with TE buffer. As the concentration of DNA increases, the solution becomes more viscous. With most of the sonication based DNA shearing methods, the viscosity has an impact on the shearing results. With our system, we have experimented with DNA sample of concen-

trations ranging from 500pg/uL to 1ug/uL and our shearing results are independent of the concentration of the DNA. This may be because of the fact that, unlike focused acoustic techniques, our phased-array transducer structure generates a distributed ultrasonic wave pattern inside the sample and that helps us in getting concentration independent shearing results. Similarly, we performed shearing experiments on DNA samples with two different starting sizes (48kb Lambda DNA and 20kb genomic DNA). In both cases, the shearing results under same experimental settings were same. This means that the shearing results are independent of the starting size of the DNA

5. **Effect of Source of DNA Sample on Shearing Results:** The shearing experiment is performed on DNA samples from two different sources to validate that the shearing process is not dependent on the type of DNA. We ran experiments on two types of DNA- Lambda DNA with 48kb base pair lengths and genomic DNA with 20kb base pairs. Under the same shearing protocol, both type of DNAs shear to same mean fragment sizes; even the size distribution around the mean is also the same. Following settings are used to get 500 base pair DNA fragments:  $V_{DC} = 73V$ , RF-frequency = 3.85MHz, Repetition Rate = 420 Hz, Number of RF Pulses in a Burst = 100. With  $V_{DC}=73V$  as supply voltage, we get around 350 volts peak-to-peak across the transducer. In this experiment, two out of four FASA elements were excited by one RF-signal and other two were driven by another RF signal at 180° out of phase with the first RF-signal. 100  $\mu L$  DNA sample, with 20ng/ $\mu L$  concentration, was put in a flat-bottom matrix orbital tube and was sonicated under the aforementioned protocol settings. Samples were aliquoted after 15 mins, 30 mins, and 1 hour of sonication. These three samples, sonicated for different time

durations, from each DNA (Lambda and Genomic) were analyzed using Lonza gel-electrophoresis system and it was found that both type of DNA sheared to equal fragment sizes. The gel image for this experiment is shown in figure-7.6.

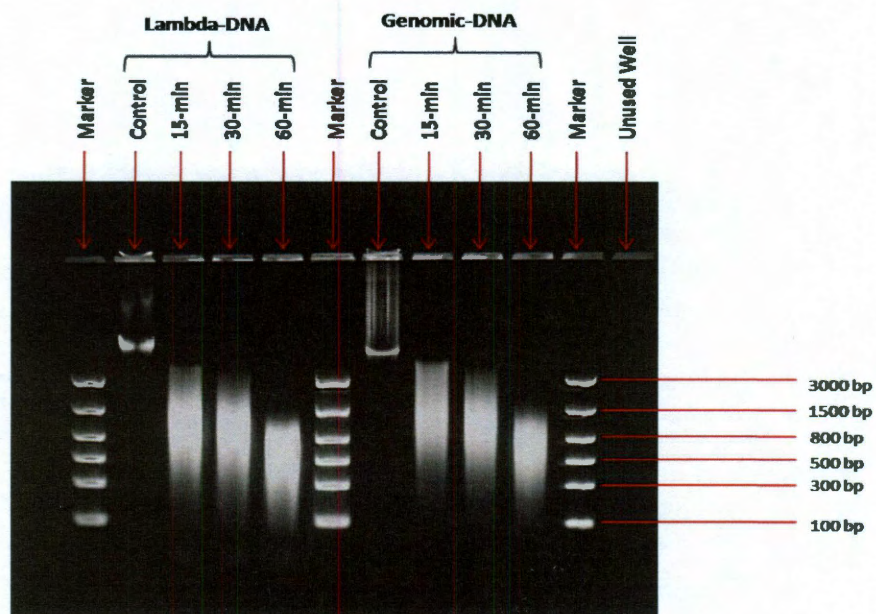


Figure 7.6 : Shearing results on Lambda and Genomic DNA for 15 mins, 30 mins, and 1 hour sonication time.

## Chapter 8

### Conclusions and Future Work

To avoid the shearing step from being a bottleneck in the sequencing process we have proposed a fast, efficient and controlled DNA shearing system in this thesis. The proposed shearing system can provide user-specified high-quality DNA fragments in significantly lesser amount of time. The system can shear DNA from any source and the shearing results are independent of concentration of input DNA. The system uses lateral acoustic shear waves to shear the DNA without damaging, heating or denaturing it. These lateral waves are generated by RF excitation of uniquely designed piezoelectric transducers.

One of the problems which we are facing today is that the transducer performance degrades over time [57, 58]. The rate of transducer performance degradation is dependent on the voltage used to excite it. The higher the voltage we apply across the transducer, the smaller the size of DNA fragments we get, but the faster the degradation of transducer. Figure-8.1 shows the log magnitude plots of  $S_{11}$  for a transducer under different usage durations. We observe that the magnitude of  $S_{11}$  minima increases with usage, which is quite surprising and is little hard to explain. One may think that the performance of transducer should increase as the  $S_{11}$  magnitude increases, but this is not the case in practice. We may explain the performance degradation through the increase in transducer selectivity as we see from the same plot in figure-8.1. By increase in selectivity, we mean that the transducer has large quality factor (Q) and it absorbs lesser frequency contents from the RF-signal. Typ-

ically, the RF-signal applied across the transducer has multiple frequencies along with the fundamental frequency. If the transducer is wide band, then large part of RF-signal (as measured by number of frequency components) will be converted in to useful acoustic energy.

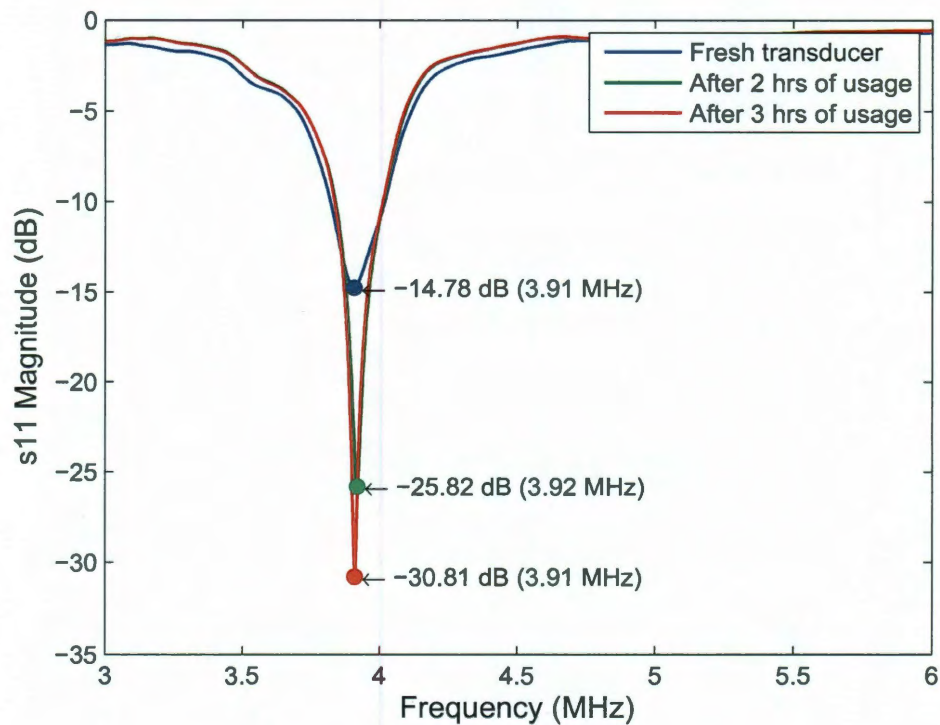


Figure 8.1 : Scattering parameter,  $S_{11}$  of FASA element after usage for different durations.

Figure-8.2 shows the resistance, reactance and impedance plots of a transducer used for different time durations. From the top plot in figure-8.2, we observe that the resistive part of impedance is increasing with its usage and it could cause more  $I^2R$  losses inside the piezoelectric plate. This in turn will increase the temperature of the transducer and will degrade the performance of the transducer. The middle plot

in figure-8.2 shows the reactance of the transducer under different usage durations. We observe that the transducer is capacitive for most of the frequencies and its capacitance increases with increased usage. The increase in capacitance will shift the resonant frequency to the higher frequency and will reduce the piezoelectric property of the material. Finally, we notice from the bottom plot that the impedance of a piezoelectric transducer increases with usage which in turn reduces the overall performance of the transducer. These problems are important to address if we want to build a commercial product and therefore, we include these problems in our future work. Once the shearing system becomes robust, we would model the shearing results with the help of fragment analysis tools, like Lonza-gel and Agilent Bioanalyzer. This would further our understanding of underlying physics behind DNA shearing [59].

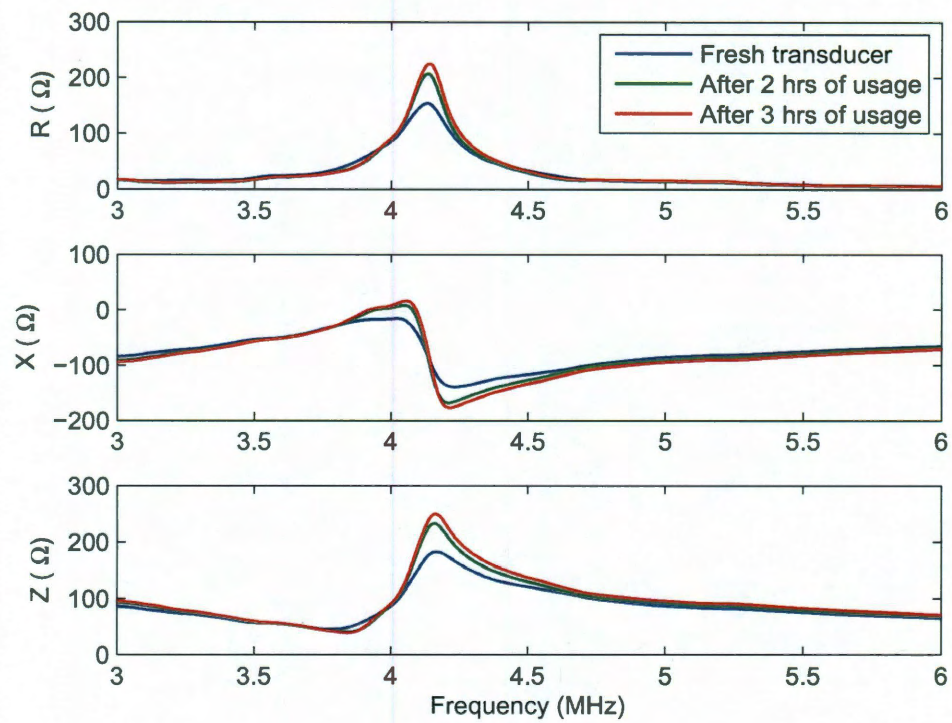


Figure 8.2 : Resistance (R), reactance (X) and impedance (Z) of FASA element after usage for different durations.



## Bibliography

- [1] T. Schoenfeld *et al.*, “The Means To An End: Optimal Methods for DNA Fragmentation and End Repair. [Online]. Available: [http://lucigen.com/store/docs/literature/eLucidations/Means\\_End.pdf](http://lucigen.com/store/docs/literature/eLucidations/Means_End.pdf)
- [2] New England BioLabs Inc. [Online]. Available: <http://www.neb.com/nebecomm/products/productM0348.asp>
- [3] Life Technologies- Invitrogen. [Online]. Available: <http://products.invitrogen.com/ivgn/product/K702505>
- [4] U.S. Department of Energy Joint Genome Institute. [Online]. Available: <http://www.jgi.doe.gov/education/how/index.html>
- [5] DIGILAB Inc. [Online]. Available: <http://www.digilabglobal.com/dnaShearing>
- [6] L. A. Schriefer *et al.*, “Low pressure DNA shearing: a method for random DNA sequence analysis,” *Nucleic Acids Research*, Vol. 18, No. 24, pp. 7455–7456, 1990.
- [7] M. Larginhoa *et al.*, “Development of a fast and efficient ultrasonic-based strategy for DNA fragmentation,” *Talanta*, vol. 81, pp. 881–886, 2010.
- [8] T. L. Mann and U. J. Krull, “The application of ultrasound as a rapid method to provide DNA fragments suitable for detection by DNA biosensors,” *Biosensors and Bioelectronics*, vol. 20, pp. 945–955, 2004.

- [9] M. L. Wu *et al.*, "Stabilization of naked and condensed plasmid DNA against degradation induced by ultrasounds and high shear vortices," *Biotechnol Applied Biochemistry*, vol. 53, pp. 237–246, 2009.
- [10] H. I. Elsner and E. B. Lindblad, "Ultrasonic Degradation of DNA," *DNA*, vol. 8, No. 10, pp. 697–701, 1989.
- [11] M. W. Miller, *et al.*, "A review of in vitro bioeffects of inertial ultrasonic cavitation from a mechanistic perspective," *Ultrasound Med. Bio.*, vol. 22, No.9, pp. 1131–1154, 1996.
- [12] K. Milowska and T. Gabryelak, "Reactive oxygen species and DNA damage after ultrasound exposure," *Biomolecular Engineering*, vol. 24, No. 2, pp. 263–267, 2007.
- [13] K. S. Suslick, *et al.*, "Acoustic cavitation and its chemical consequences," *Phil. Trans. R. Soc. Lond. A*, vol. 357, pp. 335–353, 1999.
- [14] N. J. Pritchard, *et al.*, "The ultrasonic degradation of biological macromolecules under conditions of stable cavitation. I. Theory, methods, and application to deoxyribonucleic acid," *Biopolymers*, vol. 4, No. 3, pp. 259–273, 1966.
- [15] A. R. Peacocke and N. J. Pritchard, "The ultrasonic degradation of biological macromolecules under conditions of stable cavitation. II. Degradation of deoxyribonucleic acid," *Biopolymers*, vol. 6, No. 4, pp. 605–623, 1968.
- [16] H. G. Lemaitre, *et al.*, "Fragmentation of purified mammalian DNA molecules by ultrasound below human therapeutic doses," *Human Genetics*, vol. 29, No. 1, pp. 61–66, 1975.

- [17] P. Colson, *et al.*, “Electro-optical properties of nucleic acids and nucleoproteins. V. Study of sonicated DNA and nucleohistone solutions,” *Biochim. Biophys. Acta.*, vol. 340, No. 3, pp. 244–261, 1974.
- [18] A. W. Davis and D. R. Phillips, “A Defined Molecular-Weight Distribution of Deoxyribonucleic Acid after Extensive Sonication,” *Biochem. J.*, vol. 173, pp. 179–183, 1978.
- [19] B. A. Cavic and M. Thompson, “Interfacial nucleic acid chemistry studied by acoustic shear wave propagation,” *Anal. Chim. Acta.*, vol. 469, No. 1, pp. 101–113, 2002.
- [20] S. L. Grokhovsky, “Specificity of DNA cleavage by ultrasound,” *Molecular Biology*, vol. 40, No. 2, pp. 276–283, 2006.
- [21] S. L. Grokhovsky, *et al.*, “Ultrasonic Cleavage of DNA: Quantitative Analysis of Sequence Specificity,” *Biophysics*, vol. 53, No. 3, pp. 250–251, 2008.
- [22] Y. D. Nechipurenko, *et al.*, “Characteristics of ultrasonic cleavage of DNA,” *Biophysics*, vol. 50, No. 5, pp. 1007–1013, 2009.
- [23] E. V. Rokhina, *et al.*, “Low-frequency ultrasound in biotechnology: state of the art,” *Trends Biotechnology*, vol. 27, No. 5, pp. 298–306, 2009.
- [24] H. M. Santosa and J. L. Capelo, “Trends in ultrasonic-based equipment for analytical sample treatment,” *Talanta*, vol. 73, No. 5, pp. 795–802, 2007.
- [25] M. M. Rageh, *et al.*, “Effect of high power ultrasound on aqueous solution of DNA,” *International Journal of Physical Sciences*, vol. 4, No. 2, pp. 63–68, 2009.

- [26] K. Fukudome, *et al.*, "Ultrasonic Scission of Deoxyribonucleic Acid in Aqueous Solution II. Precipitational Fractionation and Molecular Weights of Sonicated Samples," *Polymer Journal*, vol. 18, No. 1, pp. 81–88, 1986.
- [27] J. L. Dion, *et al.*, "Contamination-free high capacity converging waves sonoreactors for the chemical industry," *Ultrasonics Sonochemistry*, vol. 16, No. 2, pp. 212–220, 2009.
- [28] D. Freifelder and P. F. Davison, "Studies of sonic degradation of deoxyribonucleic acid," *Biophys. J.*, vol. 2, No. 3, pp. 235–247, 1962.
- [29] V. Vivek, Y. Zeng, and E. S. Kim, "Novel acoustic-wave micromixer," in *Proc. IEEE Int. Micro Electro Mechanical Syst. Conf.*, 2000, pp. 668–673.
- [30] V. Vivek, "Design of Acoustic Wave Micromixer Using FASA for Integration in Large Scale Fluidic MEMS," M.S. thesis, The University of Hawaii, HI, June 2000.
- [31] Microsonic Systems. [Online]. Available: <http://www.microsonics.com/>
- [32] K. Dev, V. Vivek, B. Hadimioglu, and Y. Massoud, "Analytical Modeling and Design of Ring Shaped Piezoelectric Transducers," accepted in *IEEE International Conference on Electronics, Circuits, and Systems (ICECS)*, 2011.
- [33] K. Dev, S. Sharma, V. Vivek, B. Hadimioglu, and Y. Massoud, "Design of a Scalable DNA Shearing System Using Phased-Array Ultrasonic Transducer," accepted in *IEEE International Conference on Electronics, Circuits, and Systems (ICECS)*, 2011.
- [34] K. Dev, S. Sharma, V. Vivek, B. Hadimioglu, and Y. Massoud, "Effect of Sonication Time on DNA Shearing Using Phased-Array Fresnel Annular Sector Ac-

tuator,” submitted in *IEEE International Symposium on Circuits and Systems (ISCAS)*, 2012.

- [35] Wikipedia. [Online]. Available: <http://www.wikipedia.org/>
- [36] The Science Creative Quarterly. [Online]. Available: <http://www.scq.ubc.ca/decodeing-icelands-dna/>
- [37] P. N. Hengen, “Methods and reagents: Shearing DNA for genomic library construction,” *Trends in Biochemical Sciences*, vol. 22, No. 7, pp. 273–274, 1997.
- [38] S. Surzycki, *Human Molecular Biology Laboratory*, Blackwell Publishing, 2003.
- [39] Covaris Inc. [Online]. Available: <http://www.covarisinc.com/>
- [40] Piezo Systems Inc. [Online]. Available: <http://www.piezo.com/>
- [41] J. F. Rosenbaum, *Bulk Acoustic Wave Theory and Devices*, Artech House Inc., 1988.
- [42] L. Spicci and M. Cati, “Ultrasound Piezo-Disk Transducer Model for Material Parameter Optimization,” in *Proc. COMSOL Conf. Paris*, 2010.
- [43] G. Kino, *Acoustic Waves: Design, Imaging and Analog Signal Processing*, Englewood Cliffs, NJ: Prentice-Hall, 1987.
- [44] M. I. Gutierrez, *et al.*, “Modeling the acoustic field of physiotherapy ultrasound transducers using non uniform acoustic pressure distributions,” in *Electrical Engineering, Computing Science and Automatic Control (CCE)*, 2010, pp. 256–260.

- [45] M. I. Gutierrez, *et al.*, “Finite Element Modeling of Acoustic Field of Physiotherapy Ultrasonic Transducers and the Comparison with Measurements,” in *Pan American Health Care Exchange (PAHCE)*, 2010, pp. 76–80.
- [46] X. Zu and E. S. Kim, “Microfluidic Motion Generation with Acoustic Waves,” *Sens. Actuators A, Phys*, vol. 66/1-3, pp. 355–360, 1998.
- [47] H. Yu, *et al.*, “Microfluidic Mixer and Transporter Based on PZT Self-Focusing Acoustic Transducers,” *Journal MEMS*, vol. 15, No. 4, pp. 1015–1024, 2006.
- [48] D. Huang and E. S. Kim, “Micromachined Acoustic-wave Liquid Ejector,” *Jour. MEMS*, vol. 10, pp. 442–449, 2001.
- [49] Agilent Network Analyzer. [Online]. Available: [www.agilent.com/find/E5061B](http://www.agilent.com/find/E5061B)
- [50] F. H. Raab, *et al.*, “RF and Microwave Power Amplifier and Transmitter Technologies - Part 1 to 5,” *High Frequency Electronics*, 2003.
- [51] H. Sekiya *et al.*, “Computation of design values for Class E amplifiers without using waveform equations,” *IEEE Trans. Circuits and Systems I: Fundamental Theory and Applications*, vol. 49, No. 7, pp. 966–978, 2002.
- [52] N. O. Sokal, “Class-E RF Power Amplifiers,” 2001.
- [53] M. Prokic, *Piezoelectric Transducers Modeling and Characterization*, MPI, 2004.
- [54] C. P. Ordahl, *et al.*, “Sheared DNA fragment sizing: comparison of techniques,” *Nucleic Acids Research*, vol. 3, No. 11, pp. 2985–2999, 1976.
- [55] Lonza. [Online]. Available: <http://www.lonza.com/>

- [56] Agilent 2100 Bioanalyzer. [Online]. Available: <http://www.genomics.agilent.com/>
- [57] W. P. Chen, *et al.*, "Degradation in lead zirconate titanate piezoelectric ceramics by high power resonant driving," *Materials Science and Engineering B*, vol. 99, No.1-3, pp. 203–206, 2003.
- [58] W. P. Chen, *et al.*, "Water-induced degradation in lead zirconate titanate piezoelectric ceramics," *Applied Physics Letters*, vol. 80, No.19, pp. 3587–3589, 2002.
- [59] J. F. Bithell, "Stochastic Model for the Breaking of Molecular Segments," *Journal of Applied Probability*, vol. 6, No. 1, pp. 59–73, 1969.